Spatial variability of extreme rainfall at radar subpixel scale

Authors

Nadav Peleg[1], Francesco Marra[2], Simone Fatichi[1], Athanasios Paschalis[3], Peter Molnar[1], Paolo Burlando[1]

[1]Institute of Environmental Engineering, ETH Zürich, Switzerland

[2]Department of Geography, Hebrew University of Jerusalem, Israel

[3]Faculty of the Engineering and the Environment, University of Southampton, UK

ABSTRACT

Extreme rainfall is quantified in engineering practice using Intensity–Duration–Frequency curves (IDF) that are traditionally derived from rain-gauges and more recently also from remote sensing instruments, such as weather radars. These instruments measure rainfall at different spatial scales: rain-gauge samples rainfall at the point scale while weather radar averages precipitation on a relatively large area, generally around 1 km^2. As such, a radar derived IDF curve is representative of the mean areal rainfall over a given radar pixel and neglects the within-pixel rainfall variability. In this study, we quantify subpixel variability of extreme rainfall by using a novel space-time rainfall generator (STREAP model) that downscales in space the rainfall within a

given radar pixel. The study was conducted using a unique radar data record (23 years) and a very dense rain-gauge network in the Eastern Mediterranean area (northern Israel). Radar-IDF curves, together with an ensemble of point-based IDF curves representing the radar subpixel extreme rainfall variability, were developed fitting Generalized Extreme Value (GEV) distributions to annual rainfall maxima. It was found that the mean areal extreme rainfall derived from the radar underestimate most of the extreme values computed for point locations within the radar pixel (on average, ~70%). The subpixel variability of rainfall extreme was found to increase with longer return periods and shorter durations (e.g. from a maximum variability of 10% for a return period of 2 years and a duration of 4 h to 30% for 50 years return period and 20 min duration). For the longer return periods, a considerable enhancement of extreme rainfall variability was found when stochastic (natural) climate variability was taken into account. Bounding the range of the subpixel extreme rainfall derived from radar-IDF can be of a major importance for different applications that require very local estimates of rainfall extremes.

Key words

Extreme rainfall variability; high resolution rainfall modelling; IDF curves; precipitation downscaling; sub pixel scale; weather radar

1 Introduction

Extreme rainfall is often quantified using Intensity (or Depth)–Duration–Frequency curves (IDF or DDF). IDF curves are essentially cumulative distribution functions of rainfall intensity maxima conditioned on duration, linking the rainfall maximum intensity recorded for a given duration with its return period (Coles et al., 2001; Katz et al., 2002; Koutsoyiannis et al., 1998). The recent availability of relatively long records of rainfall measurements from weather radars in a spatial and temporal resolution of ~1 km^2 and ~5 min, gives the possibility to explore the inter-gauge scale patterns and variability of extreme rainfall over large areas. A few contributions have been devoted to the use of weather radars for analyzing rainfall extremes (e.g. Allen and DeGaetano, 2005; Durrans et al., 2002; Lombardo et al., 2006; Overeem et al., 2010) and for developing IDF curves based directly on radar rainfall estimates (e.g. Eldardiry et al., 2015; Marra and Morin, 2015; Overeem et al., 2009; Paixao et al., 2015).

Rain-gauges and weather radars are recording precipitation at different spatial scales. While the former is essentially a point scale measurement, the latter refers to a volume integral scale. In fact, in most cases, the ratio between observation scales (for standard C-band radar and a standard rain-gauge) is in the order of 10^7. This means that differences between rainfall intensity for a given duration and return period are expected when comparing IDF curves developed by a rain-gauge or by a weather radar (gauge-IDF and radar-IDF from here on).

A radar-IDF curve for a given location represents the extreme of mean areal rainfall over a particular radar pixel. A single value is therefore assigned for given duration and return period to the radar pixel. The extreme rainfall expected in any

63 single point within the radar pixel cannot be estimated directly from the radar data. At
64 the same time, quantifying the uncertainty range of the radar subpixel variability of
65 extreme rainfall around the radar-IDF curve can be of major importance for applications
66 requiring local estimates of rainfall extremes; for example, the managing and designing
67 of urban drainage systems (Gires et al., 2012; Gires et al., 2013; Gregersen et al., 2013;
68 Ochoa-Rodriguez et al., 2015; Willems et al., 2012).

69 One way to estimate the extreme rainfall variability is to set a large number of
70 point-scale measuring devices (i.e., rain-gauges or disdrometers) within a weather radar
71 pixel domain, recording at the same temporal resolution of the weather radar.
72 Unfortunately this approach of recording the entire "true" extreme rainfall variability is
73 not a realistic option as numerous gauges will be required. Alternatively, the "true"
74 rainfall can be assessed using a limited number of rain-gauges interspersed within the
75 subpixel domain. The number and setup of these rain-gauges can be determined using
76 reduction methods such as the Variance Reduction Factor (Krajewski et al., 2000;
77 Morrissey et al., 1995; Peleg et al., 2013; Rodríguez-Iturbe and Mejía, 1974b; Villarini et
78 al., 2008). However, dense rain-gauge networks should have been installed a priori
79 within the area of interest, recording the same period as the weather radar.
80 Unfortunately, no such dense rain-gauge networks exist today (Krajewski et al., 2010).

81 An alternative is to estimate the ratio between the areal average rainfall and a
82 point rainfall using Areal Reduction Factors (Rodriguez-Iturbe and Mejía, 1974a;
83 Sivapalan and Blöschl, 1998; Svensson and Jones, 2010; Veneziano and Langousis, 2005).
84 The reciprocal of the reduction factor may allow a good estimation of the mean extreme

85 rainfall in one point from weather radar, but it cannot assess the extreme rainfall spatial
86 variability.

87 In this study, we explicitly quantify the radar subpixel variability of extreme
88 rainfall by using the STREAP (**S**pace-**T**ime **Re**alizations of **A**real **P**recipitation) model to
89 downscale recorded radar rainfall over a given pixel. STREAP is a novel stochastic rainfall
90 generator able to simulate high-resolution rainfall fields while preserving the rainfall
91 spatio-temporal structure and statistical characteristics (Paschalis, 2013; Paschalis et al.,
92 2014; Paschalis et al., 2013). While the model is conceived as a precipitation generator,
93 here it is essentially used only for spatial-disaggregation since the external storm
94 properties are prescribed from observations. The STREAP model is calibrated and
95 validated using a dense rain-gauge network covering the typical scale of remote-sensing
96 devices (~4 km^2). Afterwards, we use the STREAP model to downscale the radar rainfall
97 record from the pixel scale (1 km^2) to subpixel scale (10^{-4} km^2) and we estimate the
98 extreme rainfall variability of subpixels. Finally, we compute how well the temporal
99 variability of extreme rainfall that was simulated starting from the radar observations
100 represents the current stochastic (natural) climate variability by applying a
101 bootstrapping technique on the simulated record. Throughout this study we consider
102 the radar data to represent the "true" mean areal rainfall. The instrumental errors
103 related to weather radar and dense rain-gauge network data were discussed previously
104 by Peleg et al. (2013) and by Marra and Morin (2015) and are not further analyzed here.

105

2 Data

2.1 Dense rain-gauge network

A dense rain-gauge network covering an area of 4.41 km^2 was deployed in November 2011 near Kibbutz Galed (Israel), about 15 km east of the Mediterranean coastline (Fig. 1). The network has been fully described by Peleg et al. (2013) and here a brief summary is given. The network consists of 26 tipping bucket rain-gauges located at 13 different stations maintained by the Hydrometeorology Lab of the Hebrew University of Jerusalem. At each station two gauges separated by a distance of 1 m, as suggested by Ciach and Krajewski (1999) and Krajewski et al. (2003), were installed to maintain good quality control (QC). The rain-stations are non-uniformly distributed, due to the terrain limitations, with intra-distances between 57 and 2,672 m. The sampling resolution of the gauges is 1 minute, aggregated from a resolution of 0.1 mm per tip (accuracy of 3% up to 50 mm h^{-1}). To the best of our knowledge, this is the only rain-gauge network located in a Mediterranean climate, with such a high gauge density, although a few similar spatially distributed networks are located in other climates (Ciach and Krajewski, 2006; Fiener and Auerswald, 2009; Jaffrain and Berne, 2012; Jensen and Pedersen, 2005; Pedersen et al., 2010).

In this study, rainfall records collected from 1 November 2011 to 1 May 2015 are used; the total spatially averaged rainfall accumulation was 1,191 mm divided into 137 rain events. Separation between rain events was done considering a minimum of 6 hour dry period. Rain events with cumulative rainfall depth less than 0.5 mm or with fewer

than 9 stations recording rain (out of 13) are excluded. An inherent problem with tipping-bucket-gauges is that only the time at which the bucket is completely filled is recorded and no information is available on the actual period of time necessary for the filling. To overcome this problem, a backward linear interpolation to the previous recorded tip was applied (Peleg et al., 2013).

Strict QC procedures are conducted to minimize the measurement errors. Every minute the rainfall intensities measured by the two rain-gauges of each station are compared; if the difference exceeds 0.2 mm (two ticks per minute), the entire record of the station for the specific rainfall event is considered to be corrupted and is removed. The root mean square error of the rain-stations is found by

$$RMSE = \sqrt{\frac{1}{N}\sum_{i=1}^{N}\left(g^{i}_{1} - g^{i}_{2}\right)^{2}} \quad (1)$$

where *N* is the sample size and g^{i}_{1} and g^{i}_{2} are the *i-th* rain-gauge measurements of the two gauges at each rain-station, while recording rain. The RMSE found for all stations after QC is very small, in a range between 0.0278 mm min^{-1} and 0.0312 mm min^{-1} (out of the maximum error possible of 0.2 mm min^{-1}).

2.2 Weather radar

The E.M.S company weather radar system, a C-Band (5.35 cm wavelength) non-Doppler instrument, located about 63 km south of the dense rain-gauge network, is used in this study; data from this radar have been extensively used for climatological and hydrological studies in the past (Karklinsky and Morin, 2006; Marra and Morin, 2015;

147 Morin et al., 2001; Morin and Gabella, 2007; Peleg et al., 2013; Peleg and Morin, 2012;
148 Peleg and Morin, 2014; Rozalis et al., 2010). The system was deployed in the late '80s
149 and archives data since October 1990, providing almost continuous data records for 23
150 years (1990-2013). Small data gaps exist due to short periods of radar malfunction and
151 regular maintenance. The radar observation geometry is characterized by a spatial
152 resolution of 1.4° x 1 km and a temporal resolution of 5 min per volume scan.

153 Radar quantitative precipitation estimation (QPE) is obtained applying a
154 combination of (1) physically based corrections, accounting for errors due to antenna
155 pointing, ground echoes, wet radome attenuation, beam blockage, attenuation, vertical
156 profile reflectivity and (2) quantitative adjustments based on the comparison with rain-
157 gauge measurements of the official Israel Meteorological Service network, i.e. excluding
158 gauges from the network presented above (Marra and Morin, 2015; Marra et al., 2014;
159 Morin and Gabella, 2007). A fixed reflectivity to rain rate conversion Z–R relationship of
160 $Z=316R^{1.5}$ (Z in $mm^6\ m^{-3}$, R in mm h^{-1}), which follows previous radar studies over the area
161 (Morin and Gabella, 2007; Peleg and Morin, 2012), is used and the radar data are
162 converted to a 1-km^2 Cartesian grid. A detailed description of the correction procedure
163 and assessment of the accuracy of the QPE can be found in Marra and Morin (2015).

164 The analysis was conducted on a single radar pixel partly covering the area
165 sampled by the dense rain-gauge network (Domain B in Fig. 1). A total of 14,231 mm of
166 rainfall were recorded between the years 1990 and 2013 and are divided into 585 rain
167 events, i.e. an average of 24.3 mm per event.

168

169 3 Methods

170 The gap between the remote sensing scale (weather radar or satellite) and the point
171 scale (disdrometer or rain-gauge) can be bridged using downscaling approaches. Here,
172 we take advantage of the STREAP model (sub-section 3.1), a high-resolution space-time
173 rainfall generator, to stochastically downscale the observed radar rainfall. The subpixel
174 extreme rainfall variability is estimated constructing IDF curves based on the ensemble
175 of downscaled rainfall time series in multiple points. Two domains are set up for the
176 downscaling procedure (Fig. 1). Domain A is used for training, i.e., for the calibration and
177 validation of the STREAP model. This domain is composed of a network of 44,100 virtual
178 rain-gauges (simulated using the STREAP model) by discretizing the 2.1 x 2.1 km^2
179 domain into 10 x 10 m^2 pixels, covering the same domain of the actual dense rain-gauge
180 network (nearly 4 years of observations) . Domain B is used for the downscaling of
181 rainfall from the radar pixel scale to nearly point scale (Figs. 1 and 2); it is the nearest
182 radar pixel covering the gauge network. A network of 10,000 virtual rain-gauges is
183 simulated discretizing the 1 x 1 km^2 radar pixel (23 years of observations) into 10 x 10
184 m^2 pixels. A spatial scale of 10 x 10 m^2 can be considered point scale because below this
185 resolution changes in the spatial correlation of the rainfall are very small (e.g. ~0.5% for
186 a 1 min time scale, see Peleg et al., 2013) and the rainfall spatial variability is
187 substantially suppressed. The ensemble of downscaled point rainfall time series, i.e.
188 virtual rain-gauges that are simulated using the STREAP model in Domain B, is used to
189 compute the IDF curves (Fig. 2), and represents a quantitative estimate of the subpixel

190 rainfall variability (sub-section 3.2). Last, bootstrapping is applied to the simulated
191 rainfall record in order to generate samples representing the stochastic (natural) climate
192 variability, which is then compared with the single realization recorded by the radar
193 (sub-section 3.3).

194

195 3.1 Space-time stochastic rainfall model

196 The STREAP model is a rainfall generator designed for simulating high-resolution rainfall
197 fields while preserving the rainfall spatio-temporal structure and statistical properties
198 (Paschalis, 2013; Paschalis et al., 2014; Paschalis et al., 2013). It is a substantial
199 improvement of the previous works of Bell (1987) and Kundu and Bell (2003) and mainly
200 of the String of Beads model (Pegram and Clothier, 2001a; Pegram and Clothier, 2001b).
201 It is composed of three hierarchical modules: (a) a storm arrival process; (b) temporal
202 evolution of the mean areal intensity and fraction of wet area during a storm; and (c)
203 evolution of the space–time structure of rainfall during a storm.

204 3.1.1 General setting of the STREAP model

205 The STREAP model and its calibration process using weather radar products were
206 discussed in detail by Paschalis (2013) and Paschalis et al. (2013). Here we present only
207 the modifications that are made to tailor the model structure to the specific case study
208 and to set the model to a finer spatial resolution than the original application.

209 In contrast to the original STREAP model, the storm arrival process (i.e., rainfall
210 event duration and timing) is not stochastically generated as the goal here is to
211 downscale rainfall of observed storms rather than generating an ensemble of new
212 storms. We used the storm arrival sequence obtained either by the dense rain-gauge
213 network, for the domain A, or by the weather radar for the domain B.

214 The statistics of the mean areal rainfall during a storm is defined by two
215 variables: the mean areal rainfall intensity (image mean flux, IMF) and the wet area
216 fraction (WAR). Throughout the paper we use the notation introduced by Pegram and
217 Clothier (2001a) and adopted by Paschalis et al. (2013). Originally, the IMF and WAR
218 time series are simulated as a bivariate autocorrelated stochastic processes that depend
219 also on the storm duration. Here, the observed IMF time series are used as model
220 inputs, taken as the mean of the 1-min rainfall recorded by the dense rain-gauge
221 network (domain A) or as the rainfall intensity recorded by a single radar pixel (domain
222 B). As the weather radar data recorded rainfall in time intervals larger than the rain-
223 gauges (i.e., 1 min intervals), a simple linear interpolation of the rainfall intensity from
224 the radar interval to 1 min was applied. The WAR was stochastically generated using the
225 data derived from the dense rain-gauge network as explained below. This change from
226 the original model is made due to the fact that a much denser rain-gauge network is
227 required in order to estimate the WAR autocorrelation function.

228 The following changes were applied to module (b) of the original STREAP
229 scheme: (i) a variable WAR_g was generated using a Gaussian distribution $(\mu_{WAR}, \sigma_{WAR})$;

(ii) WAR autocorrelation function was defined using AR(1) model; and, (iii) WAR time series were stochastically generated following a distribution anamorphosis transformation (see for details Schleiss et al., 2009 and Schleiss et al., 2011), which couples the stochastically generated WAR_g time series to the observed IMF time series as:

$$WAR(t) = \sigma_{WAR} \cdot \left(\rho_{IW} \cdot F^{-1}\left[U\left(IMF_w(t) \right) \right] + \sqrt{1-\rho_{IW}{}^2} \cdot F^{-1}\left[U\left(WAR_g(t) \right) \right] \right) + \mu_{WAR} \qquad (2)$$

where ρ_{IW} is the correlation between WAR and IMF observed time series, $U\left(IMF_w(t)\right)$ is the Weibull quantile function for the IMF time series transformed using the two parameters of the IMF distribution $\left(\beta_{IMF}, \alpha_{IMF}\right)$, $U\left(WAR_g(t)\right)$ is the Gaussian quantile function for the WAR time series which was generated using the AR(1) model and transformed using $\left(\mu_{AR(1)}, \sigma_{AR(1)}\right)$ and F^{-1} is the Gaussian inverse cumulative probability distribution function $N \sim (0,1)$. The observed WAR was estimated by applying Thiessen polygons to every rain-station i.e., if a rain-station was recording rainfall at a given minute, its polygon was considered wet and was added to the total wet area fraction. The correlation term ρ_{IW} is estimated using the mean intensity field from rain-gauge data.

The spatial rainfall field is simulated as a probability transformation of an isotropic Gaussian random field characterized by a simple one-parameter exponential autocorrelation function. Commonly, a three-parameter exponential function is used to quantify the spatial structure of rainfall at small spatial scales (Krajewski et al., 2003;

250 Villarini et al., 2008). The rainfall spatial correlation function for the radar subpixel scale
251 was estimated using the dense rain-gauge network by Peleg et al. (2013), who obtained
252 values of C_1=0.923, C_2=3 and C_3=1 for the three-parameter exponential function at the
253 1-min scale. In this study, a simple one-parameter exponential function can be used
254 instead of the three-parameter one, as the C_3 parameter is equal to 1 and the C_1
255 parameter, that represents the measurement errors for each side-by-side rain-gauge, is
256 not accounted for and therefore is equal to 1. Additional details regarding the spatial
257 structure of rainfall in the study area and a comparison between the observed and
258 modeled spatial structures are given in Appendix A and Supplementary Material S1. The
259 equations describing the generation of the Gaussian fields using Fast Fourier Transform
260 method and the calculation of the 2-D spectrum, assuming an exponential decay of the
261 autocorrelation, can be found in Paschalis et al. (2013).

262 As in the original scheme, a lognormal function was applied to convert the
263 generated Gaussian field to the final rain field; we assume that the non-zero part of the
264 subpixel spatial rainfall distribution follows the observed lognormal distribution that is
265 recorded by the weather radar for this region (Karklinsky and Morin, 2006; Peleg and
266 Morin, 2012 and Fig. S2). The information needed for this transformation is the IMF,
267 WAR and a rainfall coefficient of variation (CV), which is a model parameter. The spatial
268 rainfall fields are correlated in time by imposing the Fourier coefficients of the Gaussian
269 fields to follow an ARMA process (i.e., temporal correlation in the Lagrangian system of
270 reference). Ideally, both the CV and ARMA parameters should be estimated using the
271 rain-gauge network, however, the rain-stations are too sparse. Therefore, the

parameters were estimated from the weather radar data and scaled to higher resolution as described in Supplementary Material S2.

The advection of the rain field is also simulated by the STREAP model. Here, we fixed the direction component to match the westerly winds, the most frequent wind direction detected for this region (Peleg and Morin, 2014), assuming that small scale structure is driven by the general flow. The speed component of the advection was generated using the Kappa distribution (Appendix B) based on the statistics presented by Peleg and Morin (2012) for this region.

3.1.2 Example of a simulated rain event

As an example of the STREAP model capability, we consider the first rain event that was recorded by the dense rain-gauge network. It started on November 15th, 2011 at 05:58 and lasted till 09:37. The total duration of the event was 220 min, during which an average of 5.6 mm of rainfall was accumulated according to the gauges. The maximum 1-min rain intensity recorded by the spatially averaged rain gauges during this event was 84 mm h^{-1}. The event is characteristic of an abrupt transition from no-rain to 50 mm h^{-1} intensity in a few minutes; typical of convective cell activity for this region (Sharon and Kutiel, 1986).

Three consecutive rainfall fields generated using the STREAP model for the first three minutes are presented in Fig. 3. The observed IMF (simulated IMF is imposed), simulated and observed max rainfall intensity (MRI) and WAR are presented in Fig. 4a. The MRI is well simulated by the model. The WAR parameter is not perfectly captured

293 but this is expected as there is a large uncertainty around the WAR estimation from
294 Thiessen polygons. An example of the variability of the maximum point rain intensity
295 that was "potentially" recordable by the 44,100 virtual rain-gauges for this event is
296 presented in Fig. 4b.

297 3.2 IDF curves computation

298 The generalized extreme value (GEV) distribution (Appendix C) is used worldwide to
299 model rainfall extremes since theoretically it is the limit distribution of block maxima of
300 iid distributed random variables following the Gumbel, Fréchet and Weibull distributions
301 (Katz et al., 2005). Following previous rainfall frequency studies based on radar data
302 (Eldardiry et al., 2015; Marra and Morin, 2015; Overeem et al., 2009; Overeem et al.,
303 2010; Paixao et al., 2015), we developed IDF curves fitting a GEV distribution to the
304 series of annual maxima. In order to keep consistency with (Marra and Morin, 2015), we
305 derive IDF curves over a single radar pixel (i.e. Domain B), corresponding to the pixel
306 overlapping with the dense rain-gauge network, focusing on 20 min, 1 h and 4 h
307 durations.

308 In this study IDF curves are developed from two different sources: (1) weather
309 radar (single pixel) representing the extremes of the areal mean precipitation; and (2)
310 each 10 x 10 m^2 grid cell corresponding to downscaled time series of rain intensity (i.e.,
311 "virtual" rain-gauges; VG from here on) representing the rainfall variability at radar
312 subpixel scale. No condition is imposed on the time concurrency of the radar and VG
313 maxima (i.e. radar maxima are not necessarily also point maxima and vice versa).

In total, 100 downscaled scenarios are stochastically generated using the STREAP model, simulating the radar subpixel rainfall variability (domain B) for the 23-years of data. We considered 100 replicates sufficient to average out the randomness of the downscaling approach. For each replicate 10,000 IDF curves representing the VG are calculated, i.e. one for each VG. Thus, for each duration (20 min, 1 h and 4 h) a total of 1,000,001 IDF curves are finally available: one representing the real weather radar and 1,000,000 representing the virtual gauges.

3.3 Bootstrapping

A bootstrapping procedure (Efron, 1979) is applied to estimate the spatio-temporal stochastic variability of the subpixel rainfall maxima. A single realization is in fact insufficient to fully analyze the stochastic (natural) climate variability of the current climate, especially for extremes. Bootstrapping has been applied many times in the past to resample natural variability (e.g., Alexander and Arblaster, 2009; Hänggi and Weingartner, 2011; Köplin et al., 2014). Bootstrapping is based on the assumption that the 23-years of data are just one possible realization out of a larger population. Here, 1,000 realizations of 23-years each are generated out of the original sample by block bootstrapping of the entire years, sampling with replacement, meaning that a specific year from the sample can appear numerous times or never in each realization. Finally, for each of the 1,000 bootstrapped realizations, 10,000 VG-IDF curves were computed.

4 Rainfall intensity validation

The STREAP model was validated using the point variability of a 1-min rain intensity as observed from the 13 pairs of real rain-gauges. For simplicity, results from one realization only are presented here.

The point variability of a 1-min rain intensity (Weibull distributed) was validated in domain A. The rain intensity distributions of the 26 observed rain-gauges and the maximum—minimum range for the rain intensity distribution that is simulated over the 44,100 virtual rain-gauges with the STREAP model across quantiles is presented in Fig. 5. For the largest part of the distribution (quantile larger than 0.3), the observed rain intensity variability was larger than the corresponding simulated one, indicating that the STREAP model slightly underestimates the rainfall variability over the domain (Fig. 5a). As a matter of fact, only one or two rain-gauges are falling outside of the simulated range. The part of the distribution representing the rainfall extreme in the domain (0.95—0.99 quantile range), which is the main interest in this study, is well represented (Fig. 5b). The only two rain-gauges which are outside the simulated range are marked in Fig. 5b along with their companion 1-m away rain-gauges, which are within the simulated range. Ideally, the two side-by-side rain-gauges should have reproduced the exact same distribution, but even after a strict QC there are small differences between the two gauges that reflect in the CDFs. This implies that the true underestimation of the STREAP rainfall variability is very small, if exists at all, and we conclude that the simulated point rainfall variability is well within the observed rainfall variability taking into account the errors in measurements of the tipping-buckets. For this reason, the

following results obtained with STREAP simulations should be regarded as a very good proxy of the real system.

5 Results and discussion

The results concerning the radar subpixel variability of extreme rainfall are presented in Figs. 6 and 7. Radar-IDF curves and the 5—95 quantile range of the VG-IDF representing the subpixel variability as computed from STREAP are presented in the main panel of Fig. 6. Cumulative distribution functions of the VG-to-radar ratio are presented for the 2, 10 and 50 years return period (upper panel of Fig. 6) and for the 20 min, 1 h and 4 h durations (right panel of the Fig. 6). In addition, the 5—95 quantile range of the ratio of the VG-to-radar IDF value for a given duration and for a given return period is presented in the lower panel of Fig. 6. Two scores are calculated for each of the cumulative distribution functions: (1) percentile of the transition point from cumulative underestimation to overestimation of the local extreme rainfall compared to the areal extreme rainfall (i.e., VG/radar equals one); and (2) interquartile range (IQR), representing the scatter of the distribution for the 25—75 quantile.

The inflection point is found to be positively dependent on the duration, increasing from a percentile value of 0.23 for the 20 min to 0.32 for the 4 h durations. A positive dependency is also noticed between the inflection point and the return period. Percentile values of 0.24, 0.28 and 0.37 are computed for the 2, 10 and 50 years return periods, respectively. Those results indicate that the extreme mean areal rainfall

intensities tend to underestimate the extreme point rainfall intensities within the subpixel area. This is the case for all durations and for all return periods and it is more evident for the lower return periods and shorter durations. In other words, comparing a randomly selected single gauge-IDF curve to a radar-IDF curve, one should expect the gauge-IDF to be higher than the radar-IDF in most of the cases. For example, for a 2-year return period there is a 76% chance for an IDF curve developed from a single rain-gauge to overestimate the radar-IDF. Overestimation (Eldardiry et al., 2015), underestimation (Marra and Morin, 2015) or "reasonable agreement" (Overeem et al., 2009; Paixao et al., 2015) relationships between a gauge-IDF and a radar-IDF are therefore all possible outcomes. The sensitivity to the selection of a rain-gauge or to its random positioning is quite large due to the considerable spatial variability of extreme rainfall at the subpixel scale. Further amelioration of radar QPE and reducing radar-gauge biases (Eldardiry et al., 2015; Marra and Morin, 2015) will likely improve the relationships between the radar-IDF and a single gauge-IDF, but of course will not eliminate the uncertainty due to the spatial (subpixel) rainfall variability.

A negative dependency is found between the IQR and the duration. The IQR values decreases from 0.081 to 0.048, comparing the 20 min and the 4 h durations. Moreover, a positive dependency between the IQR and the return period is found. The IQR values increase from 0.066 to 0.087, comparing the 2 and 50 years return periods. The IQR score directly reflects the subpixel scatter in extreme rainfall; the higher the IQR is, the higher the variability of extreme rainfall is. For example, the tails of the CDF for the 50-years return period (IQR=0.087) are much wider than the tails of the 2-years

400 return period (IQR=0.066), thus the probability of a randomly selected gauge-IDF to
401 over- or under-estimate the radar-IDF by 20% is much larger for the 50-years return
402 period. In general, the subpixel spatial scatter of extremes was found to be larger for
403 long return periods and for short durations.

404 The VG-IDF curves computed taking into account the stochastic (natural) climate
405 variability are presented in Fig. 7. This figure contains the VG-IDF curves that were
406 calculated from 100 realizations based on the annual maxima downscaled with STREAP
407 for the 23-years radar data, as in Fig. 6 (spatial stochastic variability from here on), and
408 the 1,000 realizations generated from the bootstrapped data (spatio-temporal
409 stochastic variability from here on). The rationale is to compare the subpixel spatial
410 stochastic variability with the spatio-temporal stochastic variability related to the fact
411 that IDF curves estimated from a single climatic realization, even of 23 years, are
412 expected to be relatively uncertain.

413 As in Fig. 6, the 5—95 quantile range of the subpixel variability of rainfall
414 extremes is presented for both cases (Fig. 7b). The VG 5—95 quantile range derived
415 from the spatio-temporal stochastic variability is always larger than the corresponding
416 quantile range of the spatial stochastic variability, as the spatial stochastic variability
417 represents only part of the stochastic (natural) climate variability. A simple way to
418 quantify how well the extreme subpixel rainfall variability is represented by the spatial
419 stochastic variability is by comparing the contribution of the extreme rainfall variability
420 derived from the spatial stochastic variability to the one derived from the spatio-

421 temporal stochastic variability. This was done using a spatial-to-temporal ratio score
422 (STR):

423 $$STR_{RP,D} = \left(\frac{q^{S}_{0.95} - q^{S}_{0.05}}{q^{T}_{0.95} - q^{T}_{0.05}} \right)_{RP,D} \quad (3)$$

424 The STR is computed from IDF values for each return period (*RP*) and duration (*D*) by
425 finding the ratio between the range of the VG 5—95 quantile generated using the
426 spatial stochastic variability ($q^{S}_{0.95} - q^{S}_{0.05}$)and the same range derived from the spatio-
427 temporal stochastic variability ($q^{T}_{0.95} - q^{T}_{0.05}$).

428 The STR score (an example relative to the 20 min duration is presented in Fig. 7a)
429 is found to decrease for higher return periods. This is observed for all durations. The STR
430 decrease starts around the 6 year return period, which is about one quarter of the
431 sample size (23 years). Up to this point the spatio-temporal stochastic variability of
432 extreme rainfall is well represented by the spatial stochastic variability (STR values of
433 0.95—0.99 are computed for all durations). For the 30 and 50 year return period STR
434 values of 0.74, 0.71 and 0.77, and 0.67, 0.63 and 0.71 are found for the 20 min, 1 h and
435 4 h durations (respectively). The lower estimates of the subpixel extreme rainfall
436 intensity (0.05 quantile) were very similar when the spatial and spatio-temporal
437 stochastic variability were compared (Fig. 7b). The difference between samples was
438 expressed mainly by the upper (0.95) quantile. For example, for the 50 year return
439 period a difference of 31.8, 11.4 and 1.8 mm h^{-1} was found between the spatial and the
440 spatio-temporal stochastic variability for the 20 min, 1 h and 4 h durations

441 (respectively). This implies that the role of stochastic (natural) climate variability is very
442 important and must be considered especially for long return periods and short
443 durations. The good correspondence between spatial and spatio-temporal stochastic
444 variability for short return periods suggests that a dense rain-gauge network can
445 eventually substitute a long gauge record to account for the radar subpixel variability of
446 rainfall extremes. In other words, for “ordinary” extremes (i.e., short return periods) the
447 gauge-to-gauge variability in a given radar pixel is not much dissimilar from the year-to-
448 year variability in a given long-recording gauge. However, for “infrequent” extremes
449 (i.e., long return periods) a denser spatial sampling cannot substitute for a long
450 observational period because these extreme rain intensities are likely related to very
451 specific weather patterns occurring so rarely that only a long-continuous monitoring can
452 detect their occurrence.

453 From the above results we can conclude that the subpixel variability of extreme
454 rainfall is an important feature when estimating rainfall extremes using remote sensing
455 instruments such as weather radars. In the presented case study, for a 50-year return
456 period and a 20 min duration, an extreme rainfall intensity of 150.7 mm h^{-1} would be
457 computed based on the radar-IDF only. However, a range of 133.9—194.6 mm h^{-1}
458 represents the actual variability of extreme rainfall that is expected in any specific
459 location within the radar pixel. This range is even larger (133.9—226.5 mm h^{-1}) when
460 taking the stochastic climate variability into account.

461 Explicitly addressing the extreme rainfall variability over a small spatial scale is
462 important for local impact studies. This may include studies for designing of urban

463 drainage systems that require rainfall in a higher spatial resolution than recorded by a
464 common C-band radar (Gires et al., 2012; Gires et al., 2013; Gregersen et al., 2013;
465 Ochoa-Rodriguez et al., 2015; Willems et al., 2012). Drainage system effectiveness is
466 evaluated to face extreme rainfall events using “design storms” that are typically based
467 on gauge-IDF curve data derived from a nearby location (for an extensive review see
468 Marsalek and Watt (1984) and Watt and Marsalek, 2013). Short-duration extremes are
469 often linked to small-scale convective events (García-Bartual and Schneider, 2001) that
470 are difficult to capture by a single or even with a relatively dense rain-gauge network
471 (Marra et al., 2014; Nikolopoulos et al., 2015; Nikolopoulos et al., 2014) but can be
472 captured by a weather radar (Peleg and Morin, 2012). With this analysis, we show that
473 an ensemble of design storms representing the variability of short-duration extreme
474 rainfall over a potential urban catchment can be derived by analyzing the overlying
475 radar pixels (using similar methods and tools as presented here) and using stochastic
476 rainfall generators such as STREAP to quantify uncertainties. Such a procedure will likely
477 lead to a better assessment of the drainage system effectiveness.

478

479 6 Conclusions

480 In this study we explicitly simulated the variability of extreme rainfall intensity at the
481 radar subpixel scale by applying the stochastic rainfall generator STREAP to simulate rain
482 fields with an unprecedented high spatial and temporal resolution (i.e., 10 x 10 m^2 and 1
483 min). The model was tested using a dense network of rain-gauges. IDF curves were

484 computed using the radar data and the downscaled values in order to compare rainfall
485 extremes at two different scales: the radar pixel scale (1 km^2) and the point scale (virtual
486 rain-gauges represented by the 10 x 10 m^2 gridded downscaled data). The uncertainty in
487 the variability of extreme rainfall has been fully evaluated using a bootstrapping
488 technique to address the space-time stochastic variability.

489 The key findings of this study are:

490 • Extreme rainfall derived from radar underestimates extreme rainfall computed
491 for point locations within the radar pixel for most of the pixel area. On average,
492 about 70% of the area within the radar pixel is likely underestimated using radar
493 IDFs. This underestimation is smaller for longer return periods.
494 • The subpixel variability of extreme rainfall is found to increase with longer return
495 periods and shorter durations. The maximum error in computing extreme rainfall
496 for a point location from radar for a return period of 2 years and a duration of 4
497 h can be of 10%; this error increases to 30% for 50 years return period and 20
498 min duration.
499 • The uncertainty in computing subpixel variability of extreme rainfall increases
500 when natural climate variability is taken into account. For a 23-years record, we
501 found that estimates of extreme rainfall variability for return period of 6 years or
502 less (1/4 of the radar sample) are marginally affected by natural climate
503 variability (spatial and spatio-temporal stochasticity are comparable). However,
504 for longer return periods, natural climate variability can increase uncertainty by
505 up to 16% of the estimate.

506 Neglecting radar subpixel variability of extreme rainfall can present a serious
507 shortcoming, as the extreme rainfall in a given point within the radar pixel is on average
508 at least 10% larger than the extreme rainfall estimated using the weather radar. This
509 effect can be amplified if natural climate variability is properly accounted for. We
510 therefore suggest that IDF curves directly derived from radar observations should be
511 used carefully since they do not include important sources of uncertainty, which must
512 be considered for applications requiring rainfall extremes at scales finer than the ones
513 supplied by the weather radar. In this study, we show that this can be achieved by
514 means of stochastic rainfall generators such as STREAP, which are useful tools to bridge
515 the gap between the radar and point scales and also to explore nature climate
516 variability.

517

518 **Acknowledgments**

519 The authors thank Kibbutz Galed for their valuable assistance and cooperation in setting
520 and maintaining the dense rain-gauge network. Radar data were provided by E.M.S.
521 (Mekorot Company). We thank the two reviewers (Geoffrey Pegram and a second
522 anonymous reviewer) and to András Bárdossy, the editor-in-Chief, for their significantly
523 contribution to the quality of the paper. This research was partially supported by the
524 Swiss Competence Center for Energy Research – Supply of Electricity (SCCER-SoE,
525 http://sccer-soe.ch/).

526

Appendix A – Rainfall spatial correlation

The three-parameter exponential function for a spatial correlation ρ at a separation distance h *is* described as:

$$\rho(h) = C_1 \cdot \exp\left[-\left(\frac{h}{C_2}\right)^{C_3}\right] \quad \text{(A.1)}$$

where C_1 represents the zero-distance correlation, C_2 is the correlation distance and C_3 is the shape factor. The spatial correlation function for the dense rain-gauge network in Israel was studied by Peleg et al. (2013) and values of C_1=0.923, C_2=3 and C_3=1 were computed for the 1-min scale. In this study, a simple one-parameter exponential function can be used instead of the three-parameter exponential function, as the C_3 parameter is equal to 1 and the C_1 parameter, that represents the measurement errors for each side-by-side rain-gauge (see Peleg et al. (2013) for additional information), is not accounted for and therefore can be also assumed to be equal to 1. The simulated correlation functions are not static but for each storm a new stochastic Gaussian field is generated with a different correlation. A comparison between the observed correlation function and 1,000 simulated correlograms, which were generated after calibration, are presented in Fig. A.1. The underestimation of the simulated spatial correlation for the 0—200 m distance range is due to the fact that we do not want to reproduce the correlation smaller than one at distance zero, which is most likely an artifact of the measurements error (C_1). The simulated spatial correlation correspond to mean (± standard deviation) value of C_2=2.48 (±0.31). The generated

547 fields result in a slightly faster decay than the observed spatial correlation; for example,
548 for the 2-km distance the mean observed and simulated values were $\rho_{obs}(2)=0.47$ and
549 $\rho_{sim}(2)=0.44$, respectively. The rainfall spatial correlation function was calculated using
550 the rainfall time series that was recorded by the stations. The Moran's I and Geary's C
551 indices (see Supplementary Material S1) were applied to verify that the spatial
552 correlation function is not influenced by the instantaneous rainfall intensity. By
553 estimating the mean of both indices versus the instantaneous maximum rainfall
554 intensity measured for 1-min time intervals (C≈0.6, I≈0), it was determined that no
555 dependence exists between the instantaneous maximum rainfall intensity and the
556 spatial structure of the rainfall.

557

558 **Appendix B – Kappa distribution**

559 The 4-parameter Kappa (KAP) distribution was presented by Hosking (1994). It is a
560 generalization of many other distributions and includes as special cases the Generalized
561 Logistic, GEV, and Generalized Pareto distributions. The KAP cumulative distribution
562 function $F\left(U;\xi,\alpha,k,h\right)$ are:

563 $$F\left(U;\xi,\alpha,k,h\right)=\left\{1-h\left[1-k\left(U-\xi\right)/\alpha\right]^{1/k}\right\}^{1/h} \quad \text{(A.1)}$$

564 where *U* is the wind speed, ξ is the location parameter, α is the scale parameter, and *k*
565 and *h* are the two shape parameter of the distribution. The distribution parameters are
566 estimated using L-moments following the method suggested by Hosking (Hosking and

567 Wallis, 1993; Hosking and Wallis, 1995; Hosking and Wallis, 2005). The KAP distribution
568 was generally found to provide a good fit to the wind speed in comparison to other
569 distributions (Morgan et al., 2011; Ouarda et al., 2015).

570

571 **Appendix C – GEV distribution**

572 The Generalized Extreme Values (GEV) distribution combines the Gumbel, Fréchet and
573 Weibull asymptotic extreme value distributions (Types I, II and III, respectively) into a
574 single one. The GEV cumulative distribution function $F\left(U;\mu,\sigma,\kappa\right)$ was given by
575 Jenkinson (1955):

576
$$\begin{cases} F\left(U;\mu,\sigma,\kappa\right)=\exp\left\{-\left[1-\dfrac{\kappa}{\sigma}\left(U-\mu\right)\right]^{\frac{1}{\kappa}}\right\} \ for\ \kappa\neq 0 \\ F\left(U;\mu,\sigma,\kappa\right)=\exp\left\{-\exp\left[-\dfrac{1}{\sigma}\left(U-\mu\right)\right]\right\} \ for\ \kappa=0 \end{cases} \quad \text{(B.1)}$$

577 where *U* is the rainfall intensity, μ is the location parameter, σ is the scale parameter
578 and κ is the shape parameter of the distribution. The GEV distribution parameters were
579 estimated using maximum likelihood method.

580

581

582 **References**

583 Alexander, L.V., Arblaster, J.M., 2009. Assessing trends in observed and modelled
584 climate extremes over Australia in relation to future projections. International
585 Journal of Climatology, 29(3): 417-435. DOI:10.1002/joc.1730

586 Allen, R.J., DeGaetano, A.T., 2005. Considerations for the use of radar-derived
587 precipitation estimates in determining return intervals for extreme areal
588 precipitation amounts. Journal of Hydrology, 315(1–4): 203-219.
589 DOI:http://dx.doi.org/10.1016/j.jhydrol.2005.03.028

590 Bell, T.L., 1987. A space-time stochastic model of rainfall for satellite remote-sensing
591 studies. Journal of Geophysical Research: Atmospheres, 92(D8): 9631-9643.
592 DOI:10.1029/JD092iD08p09631

593 Ciach, G.J., Krajewski, W.F., 1999. On the estimation of radar rainfall error variance.
594 Advances in Water Resources, 22(6): 585-595.
595 DOI:http://dx.doi.org/10.1016/S0309-1708(98)00043-8

596 Ciach, G.J., Krajewski, W.F., 2006. Analysis and modeling of spatial correlation structure
597 in small-scale rainfall in Central Oklahoma. Advances in Water Resources, 29(10):
598 1450-1463. DOI:http://dx.doi.org/10.1016/j.advwatres.2005.11.003

599 Coles, S., Bawa, J., Trenner, L., Dorazio, P., 2001. An introduction to statistical modeling
600 of extreme values, 208. Springer.

601 Durrans, S., Julian, L., Yekta, M., 2002. Estimation of Depth-Area Relationships using
602 Radar-Rainfall Data. Journal of Hydrologic Engineering, 7(5): 356-367.
603 DOI:10.1061/(ASCE)1084-0699(2002)7:5(356)

Efron, B., 1979. Bootstrap Methods: Another Look at the Jackknife. The Annals of Statistics, 7(1): 1-26.

Eldardiry, H., Habib, E., Zhang, Y., 2015. On the use of radar-based quantitative precipitation estimates for precipitation frequency analysis. Journal of Hydrology, 531, Part 2: 441-453. DOI:http://dx.doi.org/10.1016/j.jhydrol.2015.05.016

Fiener, P., Auerswald, K., 2009. Spatial variability of rainfall on a sub-kilometre scale. Earth Surface Processes and Landforms, 34(6): 848-859. DOI:10.1002/esp.1779

García-Bartual, R., Schneider, M., 2001. Estimating maximum expected short-duration rainfall intensities from extreme convective storms. Physics and Chemistry of the Earth, Part B: Hydrology, Oceans and Atmosphere, 26(9): 675-681. DOI:http://dx.doi.org/10.1016/S1464-1909(01)00068-5

Gires, A. et al., 2012. Quantifying the impact of small scale unmeasured rainfall variability on urban runoff through multifractal downscaling: A case study. Journal of Hydrology, 442–443: 117-128. DOI:http://dx.doi.org/10.1016/j.jhydrol.2012.04.005

Gires, A., Tchiguirinskaia, I., Schertzer, D., Lovejoy, S., 2013. Multifractal analysis of a semi-distributed urban hydrological model. Urban Water Journal, 10(3): 195-208. DOI:10.1080/1573062X.2012.716447

Gregersen, I. et al., 2013. Assessing future climatic changes of rainfall extremes at small spatio-temporal scales. Climatic Change, 118(3-4): 783-797. DOI:10.1007/s10584-012-0669-0

626 Hänggi, P., Weingartner, R., 2011. Inter-annual variability of runoff and climate within
627 the Upper Rhine River basin, 1808–2007. Hydrological Sciences Journal, 56(1):
628 34-50. DOI:10.1080/02626667.2010.536549
629 Hosking, J.R.M., 1994. The four-parameter kappa distribution. IBM J. Res. Dev., 38(3):
630 251-258. DOI:10.1147/rd.383.0251
631 Hosking, J.R.M., Wallis, J.R., 1993. Some statistics useful in regional frequency analysis.
632 Water Resources Research, 29(2): 271-281. DOI:10.1029/92WR01980
633 Hosking, J.R.M., Wallis, J.R., 1995. Correction to "Some Statistics Useful in Regional
634 Frequency Analysis". Water Resources Research, 31(1): 251-251.
635 DOI:10.1029/94WR02510
636 Hosking, J.R.M., Wallis, J.R., 2005. Regional frequency analysis: an approach based on L-
637 moments. Cambridge University Press.
638 Jaffrain, J., Berne, A., 2012. Quantification of the Small-Scale Spatial Structure of the
639 Raindrop Size Distribution from a Network of Disdrometers. Journal of Applied
640 Meteorology and Climatology, 51(5): 941-953. DOI:10.1175/JAMC-D-11-0136.1
641 Jenkinson, A.F., 1955. The frequency distribution of the annual maximum (or minimum)
642 values of meteorological elements. Quarterly Journal of the Royal
643 Meteorological Society, 81(348): 158-171. DOI:10.1002/qj.49708134804
644 Jensen, N.E., Pedersen, L., 2005. Spatial variability of rainfall: Variations within a single
645 radar pixel. Atmospheric Research, 77(1–4): 269-277.
646 DOI:http://dx.doi.org/10.1016/j.atmosres.2004.10.029

647 Karklinsky, M., Morin, E., 2006. Spatial characteristics of radar-derived convective rain
648 cells over southern Israel. Meteorologische Zeitschrift, 15(5): 513-520.
649 DOI:10.1127/0941-2948/2006/0153
650 Katz, R.W., Brush, G.S., Parlange, M.B., 2005. STATISTICS OF EXTREMES: MODELING
651 ECOLOGICAL DISTURBANCES. Ecology, 86(5): 1124-1134. DOI:10.1890/04-0606
652 Katz, R.W., Parlange, M.B., Naveau, P., 2002. Statistics of extremes in hydrology.
653 Advances in Water Resources, 25(8–12): 1287-1304.
654 DOI:http://dx.doi.org/10.1016/S0309-1708(02)00056-8
655 Köplin, N., Rößler, O., Schädler, B., Weingartner, R., 2014. Robust estimates of climate-
656 induced hydrological change in a temperate mountainous region. Climatic
657 Change, 122(1-2): 171-184. DOI:10.1007/s10584-013-1015-x
658 Koutsoyiannis, D., Kozonis, D., Manetas, A., 1998. A mathematical framework for
659 studying rainfall intensity-duration-frequency relationships. Journal of
660 Hydrology, 206(1–2): 118-135. DOI:http://dx.doi.org/10.1016/S0022-
661 1694(98)00097-3
662 Krajewski, W.F., Ciach, G.J., Habib, E., 2003. An analysis of small-scale rainfall variability
663 in different climatic regimes. Hydrological Sciences Journal, 48(2): 151-162.
664 DOI:10.1623/hysj.48.2.151.44694
665 Krajewski, W.F., Ciach, G.J., McCollum, J.R., Bacotiu, C., 2000. Initial Validation of the
666 Global Precipitation Climatology Project Monthly Rainfall over the United States.
667 Journal of Applied Meteorology, 39(7): 1071-1086. DOI:10.1175/1520-
668 0450(2000)039<1071:IVOTGP>2.0.CO;2

669 Krajewski, W.F., Villarini, G., Smith, J.A., 2010. RADAR-Rainfall Uncertainties. Bulletin of
670 the American Meteorological Society, 91(1): 87-94.
671 DOI:10.1175/2009BAMS2747.1
672 Kundu, P.K., Bell, T.L., 2003. A stochastic model of space-time variability of mesoscale
673 rainfall: Statistics of spatial averages. Water Resources Research, 39(12): n/a-n/a.
674 DOI:10.1029/2002WR001802
675 Lombardo, F., Napolitano, F., Russo, F., 2006. On the use of radar reflectivity for
676 estimation of the areal reduction factor. Nat. Hazards Earth Syst. Sci., 6(3): 377-
677 386. DOI:10.5194/nhess-6-377-2006
678 Marra, F., Morin, E., 2015. Use of radar QPE for the derivation of Intensity–Duration–
679 Frequency curves in a range of climatic regimes. Journal of Hydrology, 531, Part
680 2: 427-440. DOI:http://dx.doi.org/10.1016/j.jhydrol.2015.08.064
681 Marra, F., Nikolopoulos, E.I., Creutin, J.D., Borga, M., 2014. Radar rainfall estimation for
682 the identification of debris-flow occurrence thresholds. Journal of Hydrology,
683 519, Part B: 1607-1619. DOI:http://dx.doi.org/10.1016/j.jhydrol.2014.09.039
684 Marsalek, J., Watt, W.E., 1984. Design storms for urban drainage design. Canadian
685 Journal of Civil Engineering, 11(3): 574-584. DOI:10.1139/l84-075
686 Morgan, E.C., Lackner, M., Vogel, R.M., Baise, L.G., 2011. Probability distributions for
687 offshore wind speeds. Energy Conversion and Management, 52(1): 15-26.
688 DOI:http://dx.doi.org/10.1016/j.enconman.2010.06.015

689 Morin, E., Enzel, Y., Shamir, U., Garti, R., 2001. The characteristic time scale for basin
690 hydrological response using radar data. Journal of Hydrology, 252(1–4): 85-99.
691 DOI:http://dx.doi.org/10.1016/S0022-1694(01)00451-6
692 Morin, E., Gabella, M., 2007. Radar-based quantitative precipitation estimation over
693 Mediterranean and dry climate regimes. Journal of Geophysical Research:
694 Atmospheres, 112(D20): n/a-n/a. DOI:10.1029/2006JD008206
695 Morrissey, M.L., Maliekal, J.A., Greene, J.S., Wang, J., 1995. The Uncertainty of Simple
696 Spatial Averages Using Rain Gauge Networks. Water Resources Research, 31(8):
697 2011-2017. DOI:10.1029/95WR01232
698 Nikolopoulos, E.I., Borga, M., Creutin, J.D., Marra, F., 2015. Estimation of debris flow
699 triggering rainfall: Influence of rain gauge density and interpolation methods.
700 Geomorphology, 243: 40-50.
701 DOI:http://dx.doi.org/10.1016/j.geomorph.2015.04.028
702 Nikolopoulos, E.I. et al., 2014. Impact of uncertainty in rainfall estimation on the
703 identification of rainfall thresholds for debris flow occurrence. Geomorphology,
704 221: 286-297. DOI:http://dx.doi.org/10.1016/j.geomorph.2014.06.015
705 Ochoa-Rodriguez, S. et al., 2015. Impact of spatial and temporal resolution of rainfall
706 inputs on urban hydrodynamic modelling outputs: A multi-catchment
707 investigation. Journal of Hydrology, 531, Part 2: 389-407.
708 DOI:http://dx.doi.org/10.1016/j.jhydrol.2015.05.035

709 Ouarda, T.B.M.J. et al., 2015. Probability distributions of wind speed in the UAE. Energy
710 Conversion and Management, 93: 414-434.
711 DOI:http://dx.doi.org/10.1016/j.enconman.2015.01.036
712 Overeem, A., Buishand, T.A., Holleman, I., 2009. Extreme rainfall analysis and estimation
713 of depth-duration-frequency curves using weather radar. Water Resources
714 Research, 45(10): n/a-n/a. DOI:10.1029/2009WR007869
715 Overeem, A., Buishand, T.A., Holleman, I., Uijlenhoet, R., 2010. Extreme value modeling
716 of areal rainfall from weather radar. Water Resources Research, 46(9): n/a-n/a.
717 DOI:10.1029/2009WR008517
718 Paixao, E. et al., 2015. An integrated approach for identifying homogeneous regions of
719 extreme rainfall events and estimating IDF curves in Southern Ontario, Canada:
720 Incorporating radar observations. Journal of Hydrology, 528: 734-750.
721 DOI:http://dx.doi.org/10.1016/j.jhydrol.2015.06.015
722 Paschalis, A., 2013. Modelling the space-time structure of precipitation and its impact
723 on basin response, Zürich : ETH, 1 Band pp. DOI:10.3929/ethz-a-009917135
724 Paschalis, A., Fatichi, S., Molnar, P., Rimkus, S., Burlando, P., 2014. On the effects of
725 small scale space–time variability of rainfall on basin flood response. Journal of
726 Hydrology, 514: 313-327. DOI:http://dx.doi.org/10.1016/j.jhydrol.2014.04.014
727 Paschalis, A., Molnar, P., Fatichi, S., Burlando, P., 2013. A stochastic model for high-
728 resolution space-time precipitation simulation. Water Resources Research,
729 49(12): 8400-8417. DOI:10.1002/2013WR014437

730 Pedersen, L., Jensen, N.E., Christensen, L.E., Madsen, H., 2010. Quantification of the
731 spatial variability of rainfall based on a dense network of rain gauges.
732 Atmospheric Research, 95(4): 441-454.
733 DOI:http://dx.doi.org/10.1016/j.atmosres.2009.11.007
734 Pegram, G.G.S., Clothier, A.N., 2001a. Downscaling rainfields in space and time, using
735 the String of Beads model in time series mode. Hydrol. Earth Syst. Sci., 5(2): 175-
736 186. DOI:10.5194/hess-5-175-2001
737 Pegram, G.G.S., Clothier, A.N., 2001b. High resolution space–time modelling of rainfall:
738 the “String of Beads” model. Journal of Hydrology, 241(1–2): 26-41.
739 DOI:http://dx.doi.org/10.1016/S0022-1694(00)00373-5
740 Peleg, N., Ben-Asher, M., Morin, E., 2013. Radar subpixel-scale rainfall variability and
741 uncertainty: lessons learned from observations of a dense rain-gauge network.
742 Hydrol. Earth Syst. Sci., 17(6): 2195-2208. DOI:10.5194/hess-17-2195-2013
743 Peleg, N., Morin, E., 2012. Convective rain cells: Radar-derived spatiotemporal
744 characteristics and synoptic patterns over the eastern Mediterranean. Journal of
745 Geophysical Research: Atmospheres, 117(D15): n/a-n/a.
746 DOI:10.1029/2011JD017353
747 Peleg, N., Morin, E., 2014. Stochastic convective rain-field simulation using a high-
748 resolution synoptically conditioned weather generator (HiReS-WG). Water
749 Resources Research, 50(3): 2124-2139. DOI:10.1002/2013WR014836

750 Rodriguez-Iturbe, I., Mejía, J.M., 1974a. On the transformation of point rainfall to areal
751 rainfall. Water Resources Research, 10(4): 729-735.
752 DOI:10.1029/WR010i004p00729
753 Rodríguez-Iturbe, I., Mejía, J.M., 1974b. The design of rainfall networks in time and
754 space. Water Resources Research, 10(4): 713-728.
755 DOI:10.1029/WR010i004p00713
756 Rozalis, S., Morin, E., Yair, Y., Price, C., 2010. Flash flood prediction using an uncalibrated
757 hydrological model and radar rainfall data in a Mediterranean watershed under
758 changing hydrological conditions. Journal of Hydrology, 394(1–2): 245-255.
759 DOI:http://dx.doi.org/10.1016/j.jhydrol.2010.03.021
760 Schleiss, M., Jaffrain, J., Berne, A., 2011. Stochastic Simulation of Intermittent DSD Fields
761 in Time. Journal of Hydrometeorology, 13(2): 621-637. DOI:10.1175/JHM-D-11-
762 018.1
763 Schleiss, M.A., Berne, A., Uijlenhoet, R., 2009. Geostatistical simulation of two-
764 dimensional fields of raindrop size distributions at the meso-γ scale. Water
765 Resources Research, 45(7): n/a-n/a. DOI:10.1029/2008WR007545
766 Sharon, D., Kutiel, H., 1986. The distribution of rainfall intensity in Israel, its regional and
767 seasonal variations and its climatological evaluation. Journal of Climatology, 6(3):
768 277-291. DOI:10.1002/joc.3370060304
769 Sivapalan, M., Blöschl, G., 1998. Transformation of point rainfall to areal rainfall:
770 Intensity-duration-frequency curves. Journal of Hydrology, 204(1–4): 150-167.
771 DOI:http://dx.doi.org/10.1016/S0022-1694(97)00117-0

772 Svensson, C., Jones, D.A., 2010. Review of methods for deriving areal reduction factors.
773 Journal of Flood Risk Management, 3(3): 232-245. DOI:10.1111/j.1753-
774 318X.2010.01075.x
775 Veneziano, D., Langousis, A., 2005. The areal reduction factor: A multifractal analysis.
776 Water Resources Research, 41(7): n/a-n/a. DOI:10.1029/2004WR003765
777 Villarini, G., Mandapaka, P.V., Krajewski, W.F., Moore, R.J., 2008. Rainfall and sampling
778 uncertainties: A rain gauge perspective. Journal of Geophysical Research:
779 Atmospheres, 113(D11): n/a-n/a. DOI:10.1029/2007JD009214
780 Watt, E., Marsalek, J., 2013. Critical review of the evolution of the design storm event
781 concept. Canadian Journal of Civil Engineering, 40(2): 105-113. DOI:10.1139/cjce-
782 2011-0594
783 Willems, P., Arnbjerg-Nielsen, K., Olsson, J., Nguyen, V.T.V., 2012. Climate change
784 impact assessment on urban rainfall extremes and urban drainage: Methods and
785 shortcomings. Atmospheric Research, 103: 106-118.
786 DOI:http://dx.doi.org/10.1016/j.atmosres.2011.04.003

787

788

Figures caption

Fig 1. Map of the 2100 m x 2100 m domain of the dense rain-gauge network deployed in northern Israel (Domain A). The 13 locations where two side-by-side rain gauges are installed (blue triangles) and the 210 x 210 grid are presented in the main frame; a magnification of the grid (pixel size of 10 m x 10 m) is presented in the yellow circle. Red area represents the location of the 1000 m x 1000 m domain (Domain B). A black star marks the study area's location in Israel.

Fig 2. A schematic diagram of the methods used to estimate the subpixel extreme rainfall variability. (1) Domain A is used for the calibration and validation of the STREAP model. (2) Domain B is used for the downscaling of rainfall from the radar pixel scale to nearly point scale. (3) The downscaled point rainfall time series are used to compute the IDF curves.

Fig 3. Three consecutive rainfall fields generated using the STREAP model. The field grid is composed of 210 x 210 pixels, the dimension of each pixel is 10 m x 10 m. The fields represent the first 3 time steps of the rainfall event presented in Fig. 4.

Fig 4. Example of a rainfall event. (a) The max rainfall intensity (MRI) and the wet area ratio (WAR) simulated by STREAP (red lines) are compared with observed data (grey area); the mean areal rainfall intensity (IMF, red bars) is also shown. (b) The histogram of the simulated maximum rain intensity, as recorded by each grid point (i.e. 44,100 virtual rain gauges) for the given event is presented.

809 Fig 5. An inverse cumulative distribution function of the rain intensity that was recorded
810 and simulated over domain A. The grey lines represent the 26 rain-gauges of the dense
811 rain-gauge network. Yellow area marks the maximum and minimum rain intensity range
812 of the 44,100 virtual rain-gauges that were simulated using one realization of the
813 STREAP model. The 0.01—1 quantile is presented in (a) and the 95—99 quantile range is
814 zoomed in (b). The blue lines in (b) represent the inverse-CDF of the rain intensity that
815 were recorded by two rain-gauges located in the same station (separated by 1 m
816 distance), representing the observed maximum rain intensity. The red lines in (b)
817 represent the same, but for the minimum rain intensity range.

818 Fig 6. Analysis of IDF curve for a given radar pixel. The return periods were calculated
819 using the GEV distribution from a 23-years dataset derived from the weather radar for
820 durations of 20 min, 1 h and 4 h (purple, orange and green line, respectively). Grey areas
821 represent the 5—95 quantile range of virtual rain-gauges for each duration from 100
822 realizations that were generated using the STREAP model. Cumulative distribution
823 functions of the simulated VG-to-radar ratio for the 100 realizations are presented for
824 the 2, 10 and 50 years return period (above panel) and for the 20 min, 1 h and 4 h
825 durations (right panel). Red area represents gauge overestimation and blue area
826 represents gauge underestimation in comparison with the radar. Orange arrow points to
827 the percentile characterizing the inflection between the under- and over-estimation.
828 The interquartile range (IQR) represents the scatter of the distribution for the 25-75
829 quantile. The simulated VG-to-radar ratio for a given return period and for a given
830 duration is also presented in the lower panel of the plot.

831 Fig 7. The subpixel variability of extreme rainfall for 100 realizations based on the
832 STREAP downscaled annual maxima (spatial stochastic variability) and for 1,000
833 realizations bootstrapped to account for stochastic natural climate variability (spatio-
834 temporal stochastic variability). (a) The spatial-to-temporal ratio score (STR) for 20 min
835 duration and (b) IDF curves for the spatial (grey area) and for the spatio-temporal
836 stochastic variability (green area) are shown.

837 Fig A.1. The spatial correlation function (ρ) as a function of distance for 1-min temporal
838 scale. Observed line (dashed red) was calculated using the dense rain-gauge network
839 data (Peleg et al., 2013). Simulated lines (black) were calculated from 1,000 fields that
840 were generated with the STREAP model.

Figure 1
Click here to download high resolution image

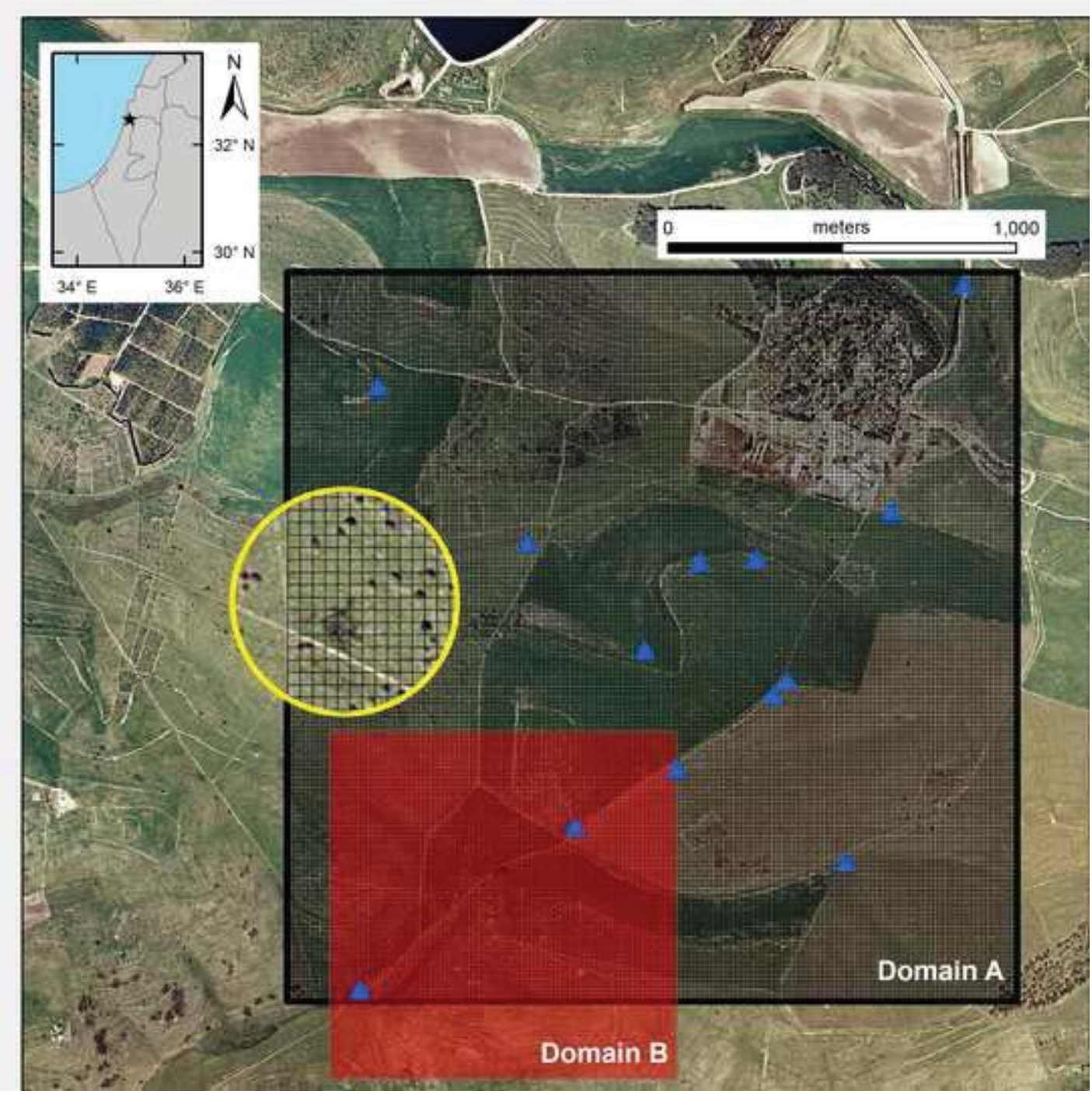

Figure 2
Click here to download high resolution image

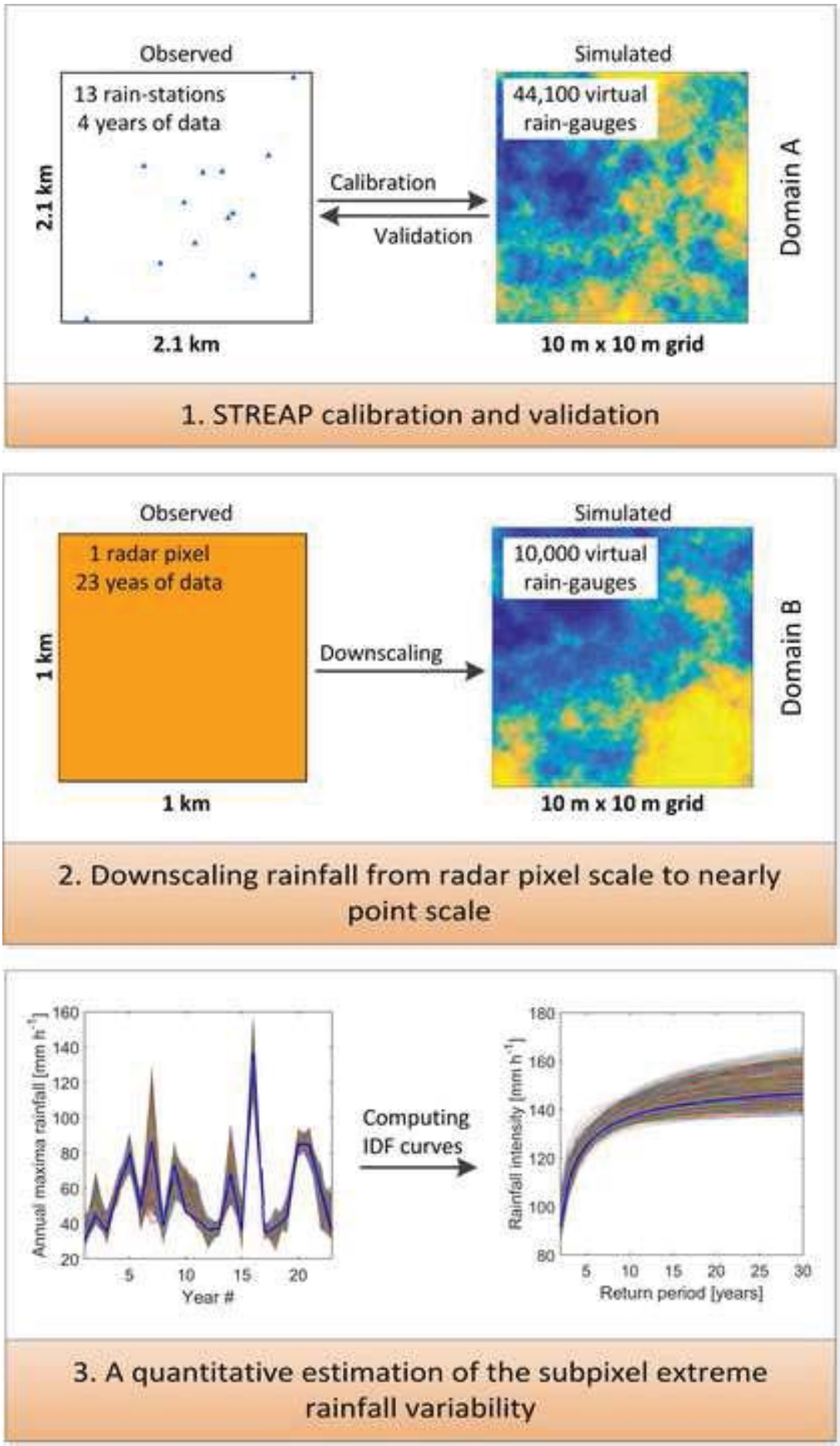

Figure 3

Click here to download high resolution image

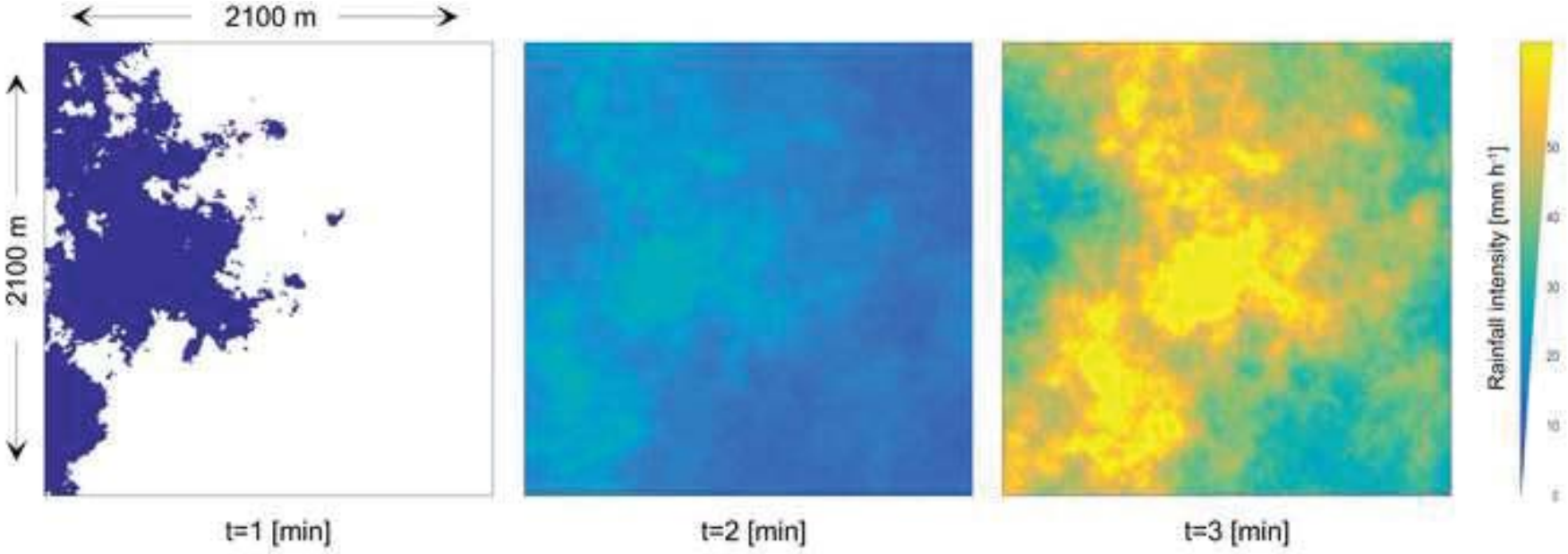

Figure 4
Click here to download high resolution image

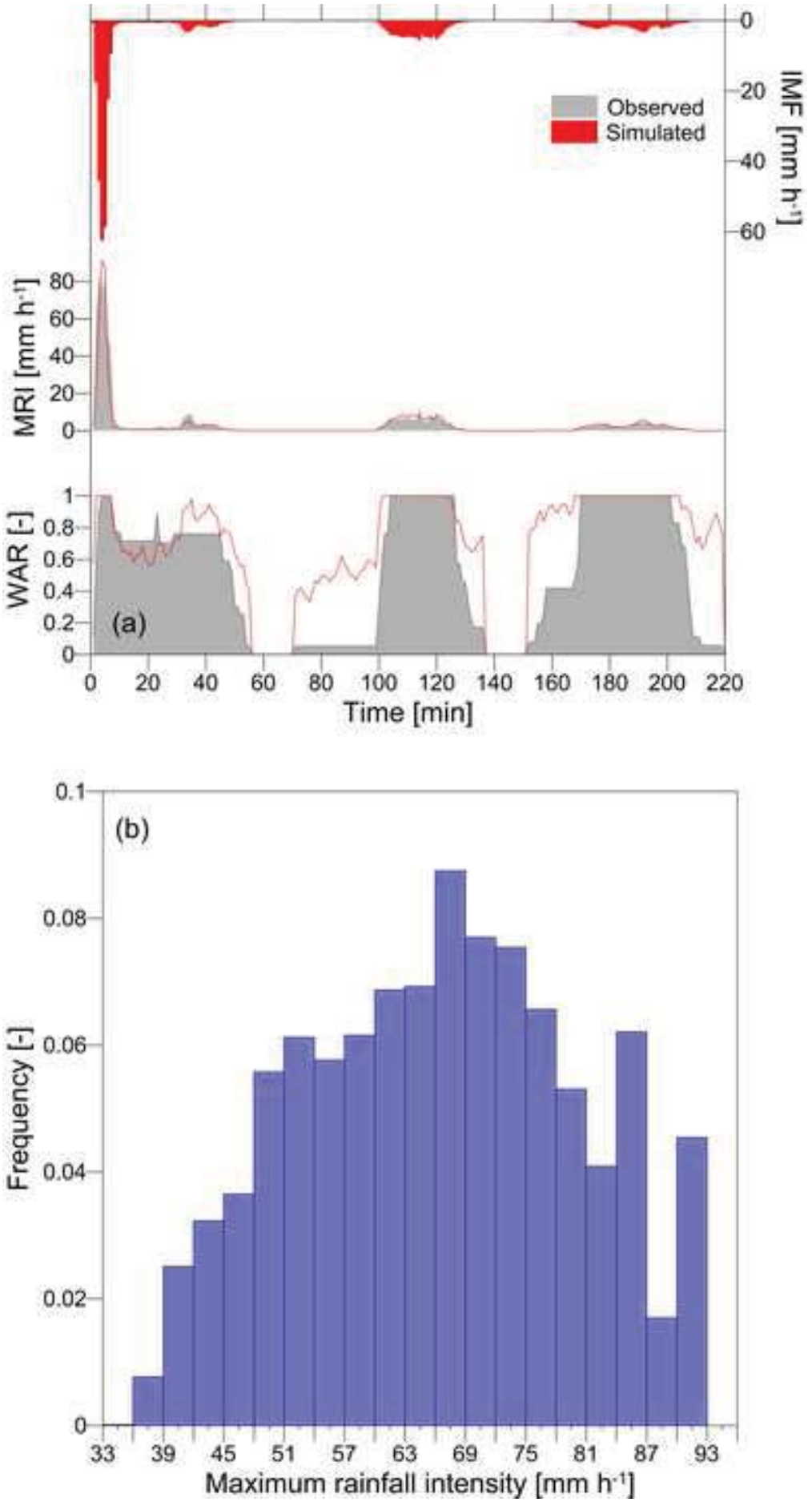

Figure 5
Click here to download high resolution image

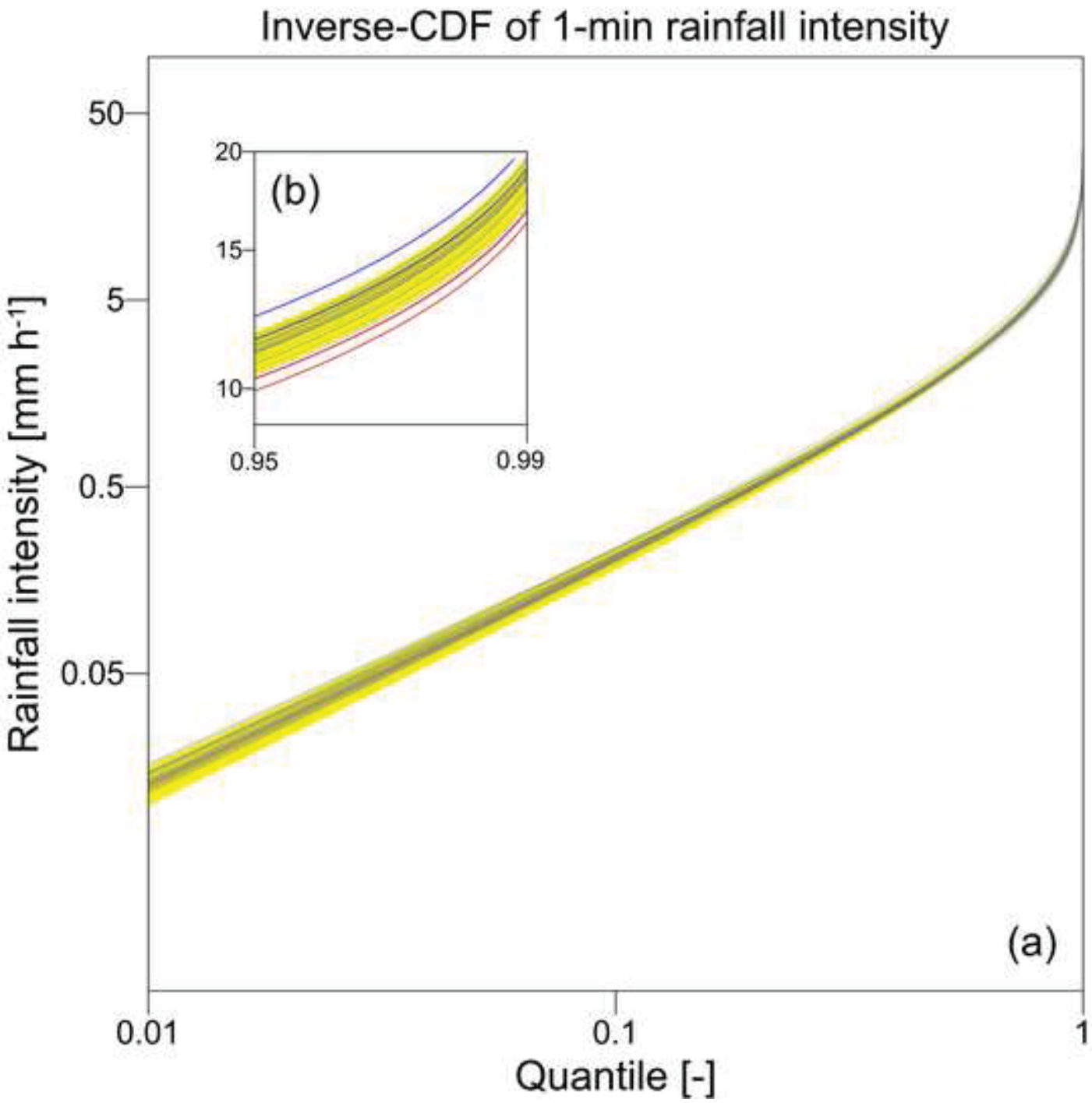

Figure 6

Click here to download high resolution image

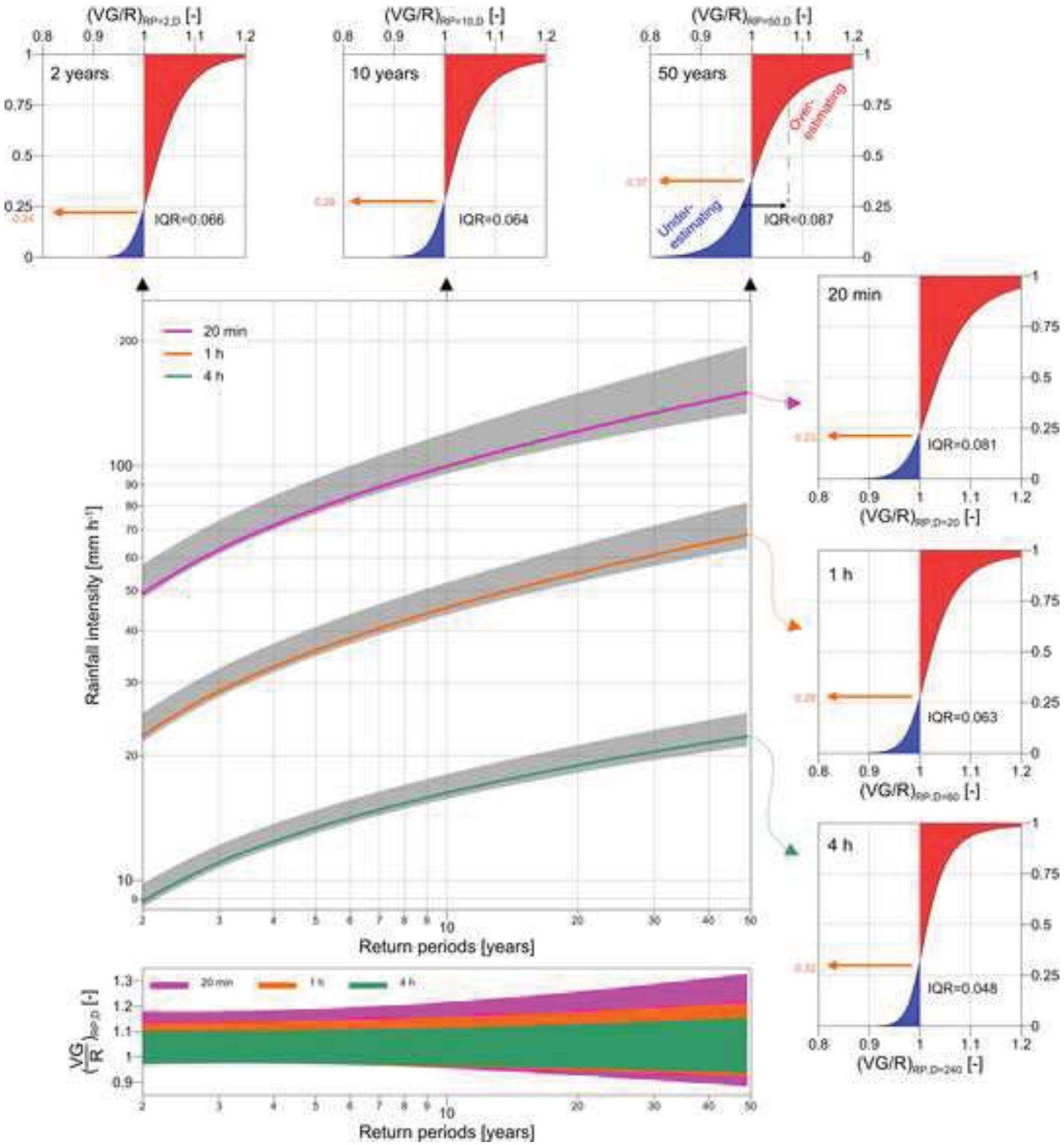

Figure 7
Click here to download high resolution image

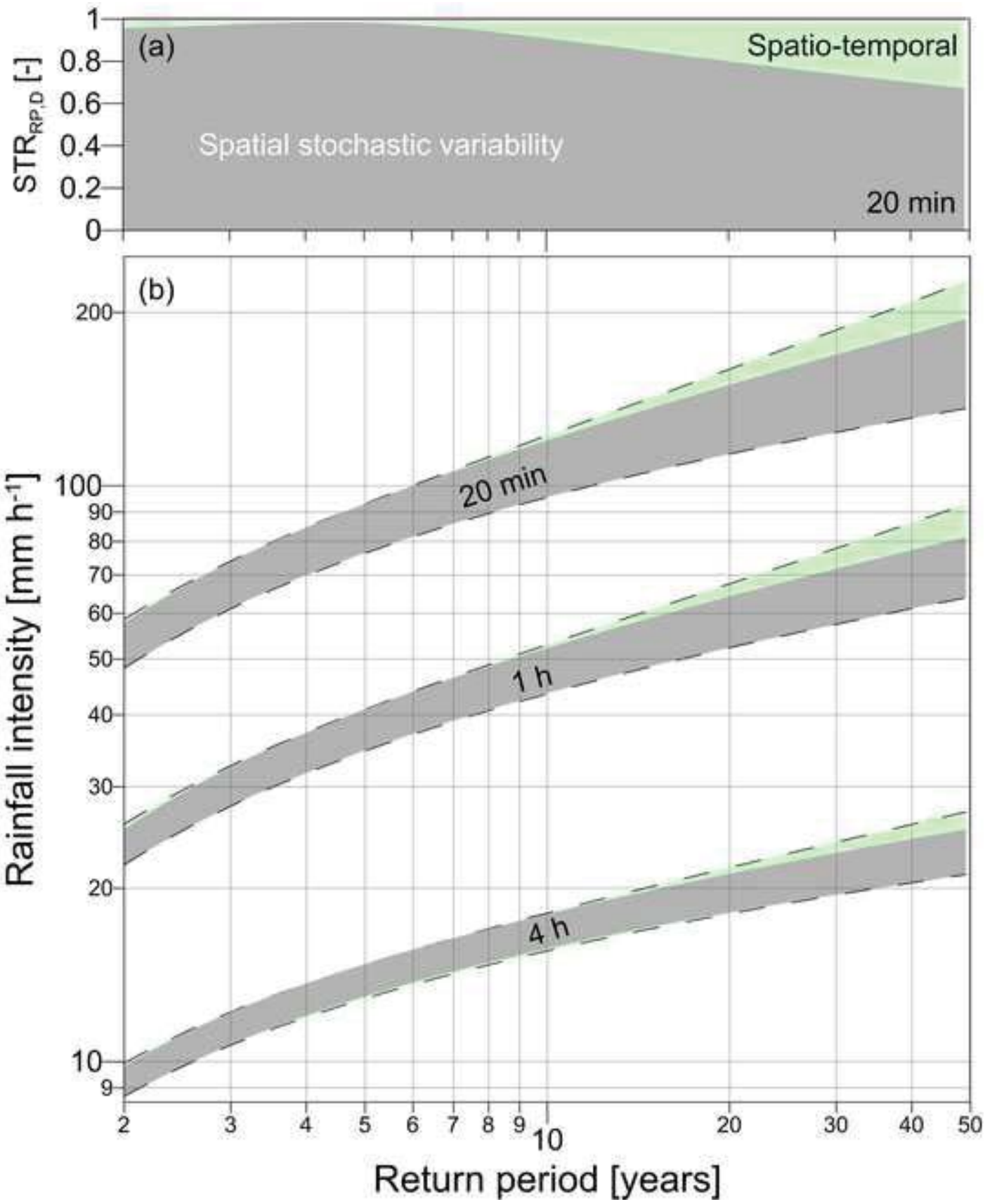

Figure A1
Click here to download high resolution image

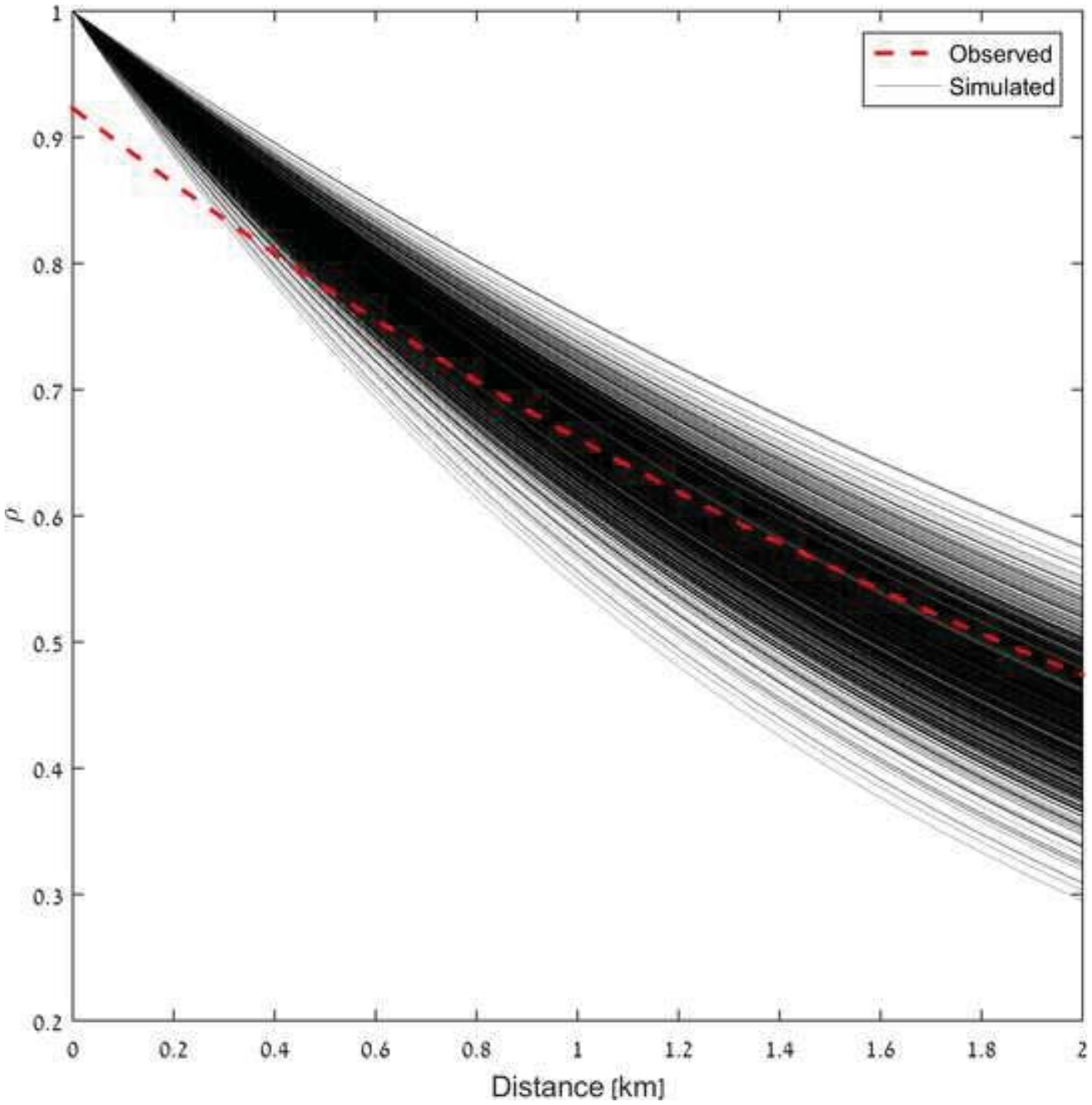

Supplementary Materials

S1 Rainfall spatial autocorrelation indices

The focus in this study is on the rainfall extreme, thus it was of important to calculate the spatial autocorrelation for each 1-min interval and evaluate it as a function of the corresponding rainfall maxima i.e., validating that the spatial structure of the rainfall is not dependent on the instantaneous maximum rain intensity.

Two indices were used to evaluate the spatial autocorrelation during a rainfall event: the Geary's C index, which is sensitive to local spatial autocorrelation (i.e., comparing rainfall intensity between rain stations), and the Moran's I index, which is sensitive to global spatial autocorrelation (i.e., comparing rain intensity between a rain-station and the mean). A summary of the two indices was given by Goodchild (1986).

The Geary's C index was given by Geary (1954):

$$C(t) = \frac{(N(t)-1)\sum_i \sum_j w_{ij}(t)\left(X_i(t) - X_j(t)\right)^2}{2\sum_i \sum_j w_{ij}(t) \sum_i \left(X_i(t) - \bar{X}(t)\right)^2} \quad \text{(S2)}$$

where t is the time step, N is the number of rain stations that were recording at time t, X_i and X_j are the rainfall intensity recorded by stations i and j accordingly, $\bar{X}$ is the mean rainfall intensity and w_{ij} is a matrix of spatial weights given in the form of the inverse distance between stations i and j.

The Moran I index was given by Moran (1948):

$$I(t) = \frac{N(t)\sum_i \sum_j w_{ij}(t)\left(X_i(t) - \bar{X}(t)\right)\left(X_j(t) - \bar{X}(t)\right)}{\sum_i \sum_j w_{ij}(t)\sum_i \left(X_i(t) - \bar{X}(t)\right)^2} \quad \text{(S3)}$$

where t, N, X_i, $\bar{X}$ and w_{ij} are equal to the one in Eq (S.2).

The value of Geary's C lies between 0 and 2, where 1 indicate no spatial autocorrelation, values smaller than 1 indicate positive spatial autocorrelation and values larger than 1 indicate negative spatial autocorrelation. The value of Moran's I lies between -1 and 1, where 0 marks no spatial autocorrelation, values larger than 0 indicate positive spatial autocorrelation and values smaller than 0 mean negative spatial autocorrelation.

The indices were calculated for the 1-min rainfall data derived from the dense rain-gauge network and then plotted against the corresponding maximum rain intensity. This was done in order to validate the assumption that the rainfall's spatial structure is not depended in the instantaneous rain intensity. The mean and standard deviation of the indices were calculated and plotted in Fig. S1 (data was binned using 3 mm h^{-1} intervals). It was found that the rainfall local spatial structure remains slightly negative (C≈0.6) while the global spatial structure indicates a spatial independence (I≈0) for the entire range of maximum rain intensities, thus no dependence was found between the instantaneous maximum rain intensity and the spatial structure of the rainfall.

S2 Estimating small scale rainfall characteristics using the weather radar

The rainfall coefficient of variation (CV) and the temporal evolution of the rainfall fields (ARMA process of rainfall field in the Lagrangian system of reference) have parameters that could not be estimated directly from the dense rain-gauge network. For the CV estimation an even denser network of rain-gauges would be required within the domain to better represent the rainfall standard deviation, while for estimating the temporal evolution of the rainfall field a gridded rainfall data for the domain would be required. The parameters of the ARMA model and CV were estimated using the weather radar.

The rainfall CV was calculated for domain areas ranging from 6-60 km^2 around the rain-gauge network (Fig. S3). Using similar scaling concept as suggested by Schleiss et al. (2011), a power function of $CV=0.13*Area^{0.38}$ was fitted to the data with an R^2 value of 0.95 and from this function an estimated CV of 0.13 was extrapolated for the 1 km^2 domain. Note that the sub-domain grid used to compute the spatial CV is the same for all domain areas and fixed by the radar resolution (1 km^2). A similar decrease of rainfall CV as a function of domain area was presented by Sassi et al. (2014). Although the rain-gauges are likely too sparse, an assessment of the CV derived directly from the rain-gauge network yield an estimated CV of 0.23. Therefore, the range of rainfall CV was set between 0.13 and 0.23.

The temporal evolution of the rainfall field is following the field motion. Estimating the ARMA parameters is a difficult and uncertain task. The advection of the rainfall field (field velocity and direction) are not stationary over time and the rainfall field is prone to rotation, convergence and divergence. Paschalis (2013) suggested to use a storm tracking algorithm to identify storms that are moving approximately constantly and then to

estimate the ARMA parameters by using a constrained least square fitting procedure of the theoretical autocorrelation function of the ARMA process. Paschalis et al. (2013) used an ARMA(2,2) model for rainfall data analyzed in Switzerland, but stated that different orders of the ARMA model are expected in other locations. In order to estimate the ARMA process for the domains A and B (i.e., for 1-min and 4 km^2 or 1 km^2, respectively) we used Paschalis (2013) estimating procedure for the weather radar data (5-min temporal resolution and 16-57 km^2 spatial resolution); the results of the first 5 spatial scales are presented in Fig. S3. Smaller scales cannot be examined, as not enough data would be available for a proper estimation. For the smallest scales that were examined (16-20 km^2) an autocorrelation value of 0.9 for all spatial lags was computed. We therefore expect that the autocorrelation function will show similar or higher values for the smaller domains. Here, we assume an AR(1) model with correlation coefficient in the range 0.85—0.95.

References

Geary, R.C., 1954. The Contiguity Ratio and Statistical Mapping. The Incorporated Statistician, 5(3): 115-146. DOI:10.2307/2986645

Goodchild, M.F., 1986. Spatial autocorrelation, 47. Geo Books.

Moran, P.A.P., 1948. The Interpretation of Statistical Maps. Journal of the Royal Statistical Society. Series B (Methodological), 10(2): 243-251. DOI:10.2307/2983777

Paschalis, A., 2013. Modelling the space-time structure of precipitation and its impact on basin response, Zürich : ETH, 1 Band pp. DOI:10.3929/ethz-a-009917135

Paschalis, A., Molnar, P., Fatichi, S., Burlando, P., 2013. A stochastic model for high-resolution space-time precipitation simulation. Water Resources Research, 49(12): 8400-8417. DOI:10.1002/2013WR014437

Peleg, N., Morin, E., 2012. Convective rain cells: Radar-derived spatiotemporal characteristics and synoptic patterns over the eastern Mediterranean. Journal of Geophysical Research: Atmospheres, 117(D15): n/a-n/a. DOI:10.1029/2011JD017353

Peleg, N., Ben-Asher, M., Morin, E., 2013. Radar subpixel-scale rainfall variability and uncertainty: lessons learned from observations of a dense rain-gauge network. Hydrol. Earth Syst. Sci., 17(6): 2195-2208. DOI:10.5194/hess-17-2195-2013

Sassi, M.G., Leijnse, H., Uijlenhoet, R., 2014. Sensitivity of power functions to aggregation: Bias and uncertainty in radar rainfall retrieval. Water Resources Research, 50(10): 8050-8065. DOI:10.1002/2013WR015109

Schleiss, M., Jaffrain, J., Berne, A., 2011. Statistical analysis of rainfall intermittency at small spatial and temporal scales. Geophysical Research Letters, 38(18): n/a-n/a. DOI:10.1029/2011GL049000

Figures caption

Fig S1. Geary's C and Moran's I indexes as a function of 1-min maximum rain intensity. The value of Geary's C lies between 0 and 2 (1 - no spatial autocorrelation, <1 positive spatial autocorrelation and >1 negative spatial autocorrelation). The value of Moran's I lies between -1 and 1 (0 - no spatial autocorrelation, >0 positive spatial autocorrelation and <0 negative spatial autocorrelation). The numbers above the points represent the number of observations in each bin.

Fig S2. Lognormal distribution fitted to the rainfall intensity on a typical convective radar image [22/12/1999 22:50, data obtained from the analysis presented by Peleg and Morin (2012)].

Fig S3. Rainfall coefficient of variation (CV) and temporal correlation coefficient (AR(1)) fit and prediction at different spatial scales as obtained from the weather radar.

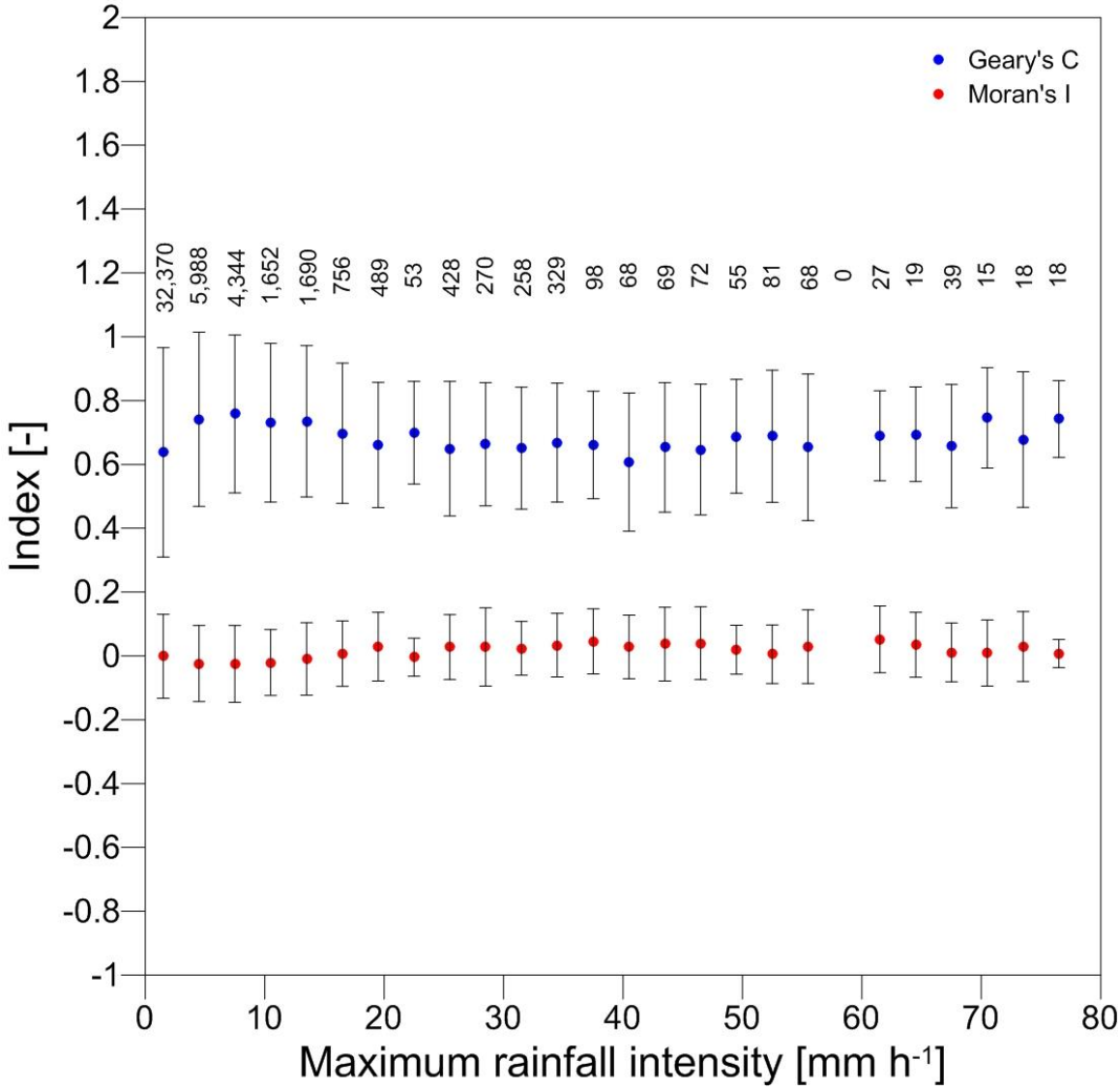
Geary's C
Moran's I
32,370
5,988
4,344
1,652
1,690
756
489
53
428
270
258
329
98
68
69
72
55
81
68
0
27
19
39
15
18
18
Index [-]
Maximum rainfall intensity [mm h-1]

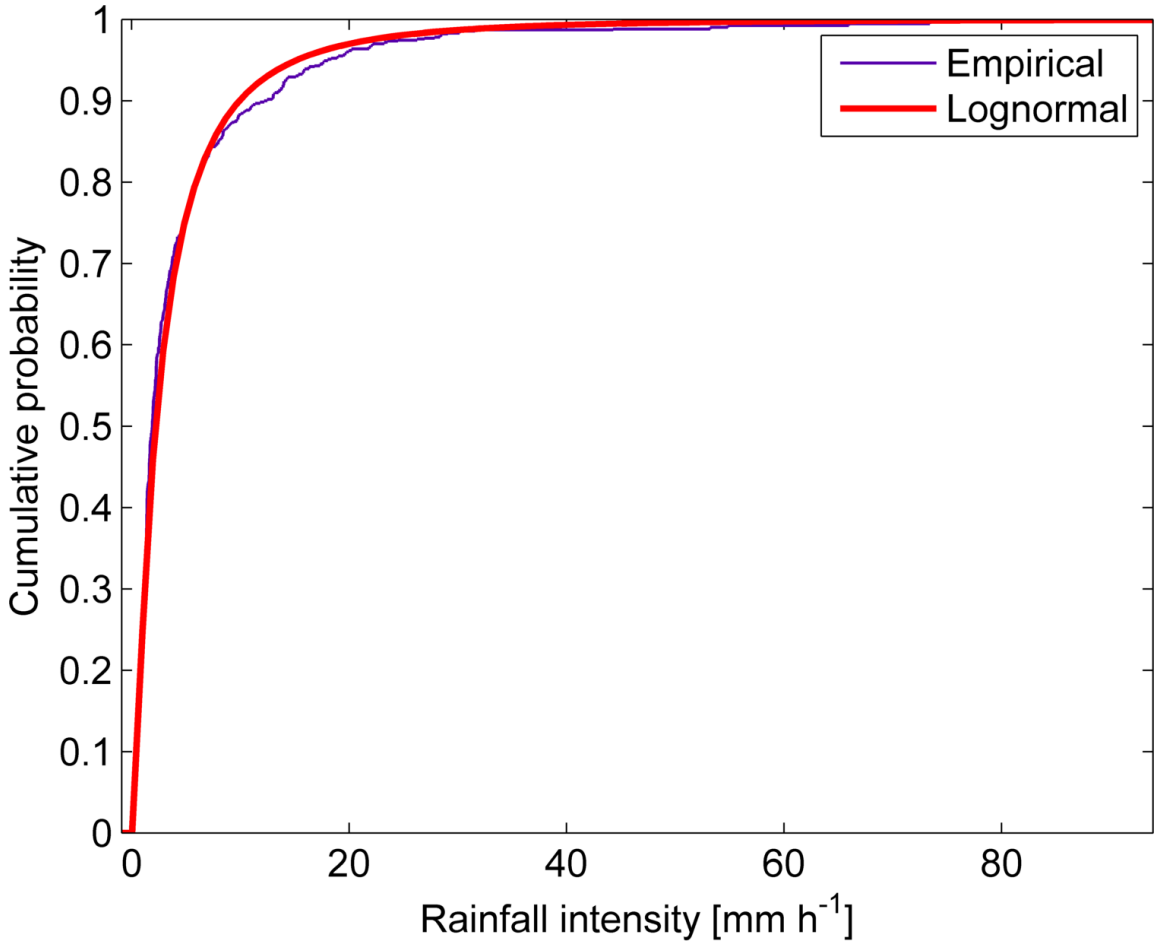
Empirical
Lognormal
Cumulative probability
Rainfall intensity [mm h-1]
0
0.1
0.2
0.3
0.4
0.5
0.6
0.7
0.8
0.9
1
0
20
40
60
80

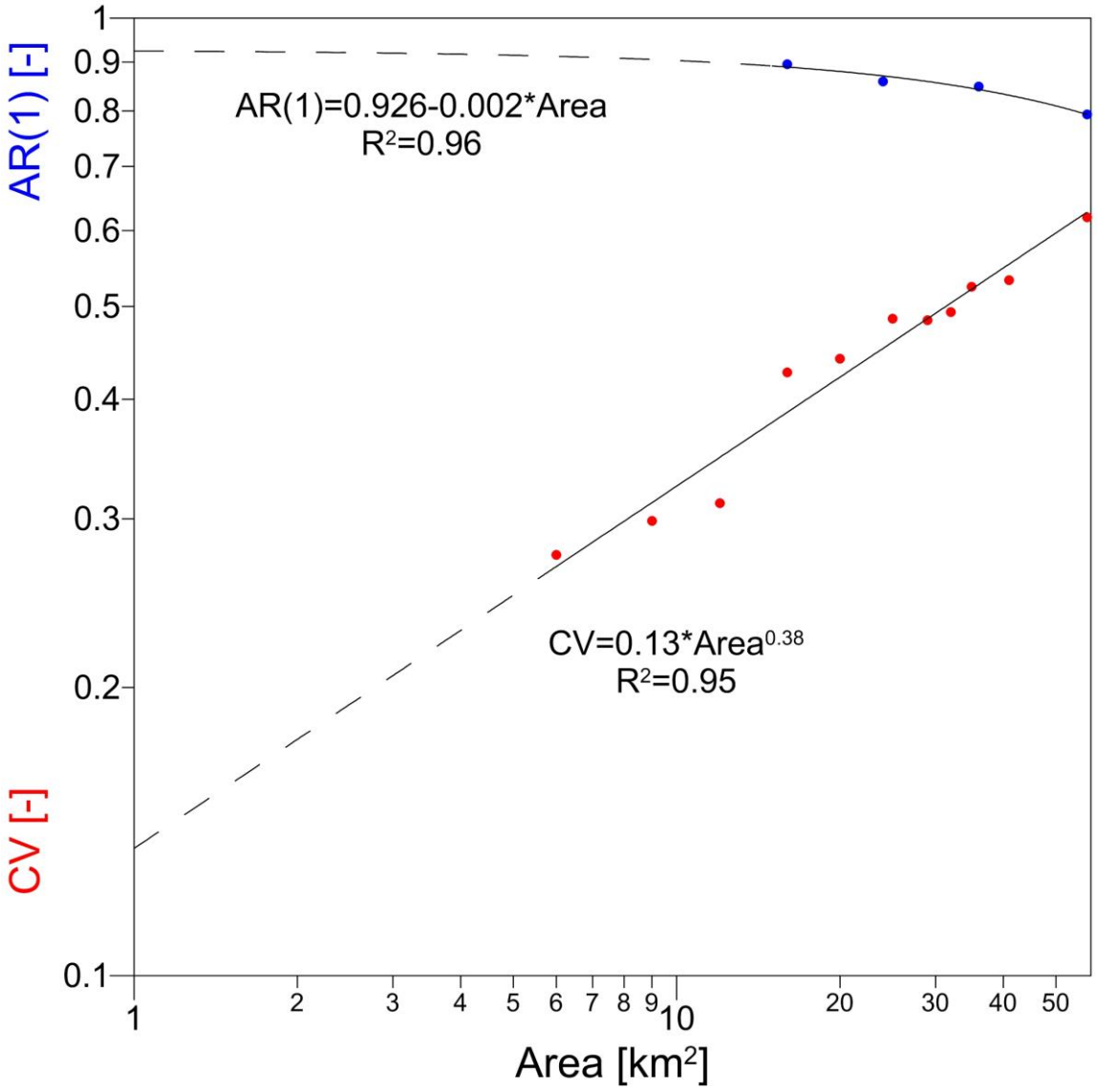
AR(1) [-]
CV [-]
AR(1)=0.926-0.002*Area
R²=0.96
CV=0.13*Area^0.38
R²=0.95
Area [km²]
1
0.9
0.8
0.7
0.6
0.5
0.4
0.3
0.2
0.1
1
2
3
4
5
6
7
8
9
10
20
30
40
50